

From galactic nuclei to the halo outskirts: tracing supermassive black holes across cosmic history and environments

David Izquierdo-Villalba,¹★ Silvia Bonoli,^{2,3} Massimo Dotti,^{4,5} Alberto Sesana,⁴
 Yetli Rosas-Guevara,² Daniele Spinoso¹

¹ *Centro de Estudios de Física del Cosmos de Aragón (CEFCA), Plaza San Juan 1, Planta-2, Teruel, 44001, Spain.*

² *Donostia International Physics Centre (DIPC), Paseo Manuel de Lardizabal 4, 20018 Donostia-San Sebastian, Spain*

³ *IKERBASQUE, Basque Foundation for Science, E-48013, Bilbao, Spain*

⁴ *Dipartimento di Fisica “G. Occhialini”, Università degli Studi di Milano-Bicocca, Piazza della Scienza 3, 20126 Milano, Italy*

⁵ *INFN, Sezione Milano-Bicocca, Piazza della Scienza 3, I-20126 Milano, Italy*

Accepted XXX. Received YYY; in original form ZZZ

ABSTRACT

We study the mass assembly and spin evolution of supermassive black holes (BHs) across cosmic time as well as the impact of gravitational recoil on the population of nuclear and wandering black holes (wBHs) by using the semi-analytical model **L-Galaxies** run on top of **Millennium** merger trees. We track spin changes that BHs experience during both coalescence events and gas accretion phases. For the latter, we assume that spin changes are coupled with the bulge assembly. This assumption leads to predictions for the median spin values of $z = 0$ BHs that depend on whether they are hosted by pseudobulges, classical bulges or ellipticals, being $\bar{a} \sim 0.9, 0.7$ and 0.4 , respectively. The outcomes of the model display a good consistency with $z \leq 4$ quasar luminosity functions and the $z = 0$ BH mass function, spin values and black hole-bulge mass correlation. Regarding the wBHs, we assume that they can originate from both the disruption of satellite galaxies (*orphan* wBH) and ejections due to gravitational recoils (*ejected* wBH). The model points to a number density of wBHs that increases with decreasing redshift, although this population is always ~ 2 dex smaller than the one of nuclear black holes. At all redshifts, wBHs are typically hosted in $M_{\text{halo}} \gtrsim 10^{13} M_{\odot}$ and $M_{\text{stellar}} \gtrsim 10^{10} M_{\odot}$, being *orphan* wBHs the dominant type. Besides, independently of redshift and halo mass, *ejected* wBHs inhabit the central regions ($\lesssim 0.3R_{200}$) of the host DM halo, while *orphan* wBHs linger at larger scales ($\gtrsim 0.5R_{200}$). Finally, we find that gravitational recoils cause a progressive depletion of nuclear BHs with decreasing redshift and stellar mass. Moreover, ejection events lead to changes in the predicted local black hole-bulge relation, in particular for BHs in pseudobulges, for which the relation is flattened at $M_{\text{bulge}} > 10^{10.2} M_{\odot}$ and the scatter increase up to ~ 3 dex.

Key words: galaxies:theoretical – galaxies:black holes – galaxies:quasar – methods:numerical

1 INTRODUCTION

Since the discovery of the first quasar (Schmidt 1963) our understanding of supermassive black holes (BHs), their growth and relation with the host galaxies has substantially increased, although a complete and exhaustive picture on their formation, evolution and impact on the environment is still missing. A couple of decades ago, observational results con-

firmed both the existence of BHs at the center of most massive galaxies and the presence of a correlation between their masses and the properties of their hosts (Soltan 1982; Haehnelt & Rees 1993; Faber 1999; O’Dowd et al. 2002; Häring & Rix 2004; Kormendy & Ho 2013; Savorgnan et al. 2016). Their effect on shaping the star formation of their hosts has also been extensively studied (Silk & Rees 1998; Birzan et al. 2004; Diamond-Stanic & Rieke 2012; Mullaney et al. 2012a,b; Eisenreich et al. 2017). Observational studies are finally finding direct evidence of AGN-driven winds

★ E-mail: dizquierdo@cefca.es

(Tombesi et al. 2014, 2015; Cresci et al. 2015; Bischetti et al. 2017).

From a theoretical point of view, it is well established that black holes grow via gas accretion and coalescence with other black holes (Marulli et al. 2008; Bonoli et al. 2016; Hirschmann et al. 2012, 2014; Fanidakis et al. 2011; Dubois et al. 2012). While the former seems to be the main contributor to the total mass-assembly budget (Soltan 1982), the latter appears to have just a sub-dominant importance (Small & Blandford 1992; Fanidakis et al. 2011; Dubois et al. 2014). Concerning gas accretion, several physical processes are believed to be responsible for driving gas towards the black hole surroundings. One of these processes is galaxy mergers, whose gravitational torques can modify the galaxy cold gas structure and trigger gas inflows towards the nuclear region (Hernquist 1989; Barnes & Hernquist 1991; Mihos & Hernquist 1996; Di Matteo et al. 2005; Springel 2005; Li et al. 2007). Secular processes such as the formation of bar structures or the redistribution of gas after supernovae explosions may have similar effects (Shlosman et al. 1989; Hopkins et al. 2009; Hopkins & Quataert 2010; Fanali et al. 2015; Dubois et al. 2015; Du et al. 2017). However, no clear observational conclusions about these two latter feeding mechanisms have been reached up to date. After being transported towards the nuclear parts, the gas has to lose a significant amount of its angular momentum to reach closer orbits around the BH to be ultimately accreted by it. Even though this process is not trivial and probably does not have an unique answer, many works have pointed out that both *local viscous stress* and *gravitational torques* (such as bars-within-bars, spiral waves or large-scale magnetic stress) can be very effective in transporting gas close to the BH ($\lesssim 0.01 - 0.1$ pc) before being transformed into stars (Shlosman & Begelman 1989; Balbus & Hawley 1998; Thompson et al. 2005).

As a result of gas accretion onto the BHs, a large amount of energy can be released prompting the birth of a *quasar* or an *Active Galactic Nucleus* (Soltan 1982; Hopkins et al. 2007; Ueda et al. 2014). The amount of energy released depends on the mass of the black hole, the geometry of the accretion disk and on the spin of the black hole (Shakura & Sunyaev 1973; Merloni & Heinz 2008). The dimensionless *spin* parameter, a , is defined as: $a = cJ_{\text{BH}}/GM_{\text{BH}}^2 \lesssim 1$ where c is the speed of light, G is the gravitation constant and J_{BH} is the black hole angular momentum. Its specific value plays an important role in the BH assembly and feedback. While highly-spinning BHs can convert up to $\sim 40\%$ of the accreted matter into radiation, slowly spinning ones can only reach up to $\sim 5\%$. This translates into potentially very bright radiative emission and relatively slow mass-growth of the first ones, as opposed to the generally high growth-rates and low luminosity of the latter ones (Bardeen 1970; Novikov & Thorne 1973; Page & Thorne 1974). Moreover, the production and strength of AGN jets might be related to the value of the BH spin (Blandford & Znajek 1977). How BHs acquire their spin is not fully understood yet. Up to date, all the proposed theories have assumed that a BH reaches its final spin after repeated gas accretion episodes and BHs coalescence that modify the initial rotation (Fanidakis et al. 2011; Volonteri et al. 2013; Berti & Volonteri 2008; Barausse 2012). On the

gas accretion side, several theoretical scenarios have been proposed. For instance, King et al. (2005) suggested the *chaotic* scenario where the gas accretion always proceeds via consumption of self-gravitating accretion disks in uncorrelated directions. In this scenario, BHs tend to spin-down towards a typical final value of $a \lesssim 0.2$ (King et al. 2008). On the other side, Volonteri et al. (2007) showed that a *prolonged* gas accretion in the form of a constant and coherent gas consumption, efficiently spins-up the BHs up to $a \sim 1$. These two can be seen as extreme cases, and intermediate scenarios have been explored (see e.g. Dotti et al. 2013; Fiacconi et al. 2018; Bustamante & Springel 2019). Over the last years, some works have attempted to measure BHs spin by using X-ray spectroscopy (Brenneman & Reynolds 2006; Reynolds 2013). However, the challenges and biases in the observations make it difficult to draw solid conclusions. In the near future, with the upcoming experiments such as *Laser Interferometer Space Antenna* (LISA, Amaro-Seoane et al. 2017) or *Advanced Telescope for High-ENergy Astrophysics* (ATHENA, Nandra et al. 2013) it will be possible to reach robust observational conclusions ruling out many theoretical models of BH spin evolution.

Even though BH-BH coalescences seem to play a sub-dominant role in the evolution of both BH mass and spin, they can have an important effect on the co-evolution between black hole and galaxy (Redmount & Rees 1989). Because of conservation of linear momentum, the propagation of gravitational waves imparts a recoil (or *kick*) in the remnant BH (Bekenstein 1973; Baker et al. 2008; Lousto et al. 2012). Small kicks could simply lead to a small displacement of the remnant BH from the galaxy center whose observational counterpart would be an offset AGN (Madau & Quataert 2004; Loeb 2007; Blecha & Loeb 2008b; Guedes et al. 2011). At the other extreme, if the recoil velocity is larger than the escape velocity of its host galactic center, the black hole can be *kicked out* of the galaxy becoming a *wandering* black hole. This last case could be more probable at high- z , where the galaxy potential wells are smaller and relatively small recoil kicks can effectively expel the BH from the galaxy and possibly even from the halo potentials. Such BH ejections might have some important consequences to be taken into account when drawing a complete black hole-galaxy co-evolution picture. For instance Blecha et al. (2011), by using hydrodynamical simulations, found that the bulge velocity dispersion and the BH mass relation changes (a shift in the velocity dispersion axis) when the simulation is run with and without the inclusion of recoil velocities. This deviation is due to the fact that the ejection interrupts the BH growth while the galaxy continue its evolution (see similar results of Blecha & Loeb 2008a; Gerosa & Sesana 2015). In the same work, Blecha et al. (2011) discussed the halting of AGN feedback as a consequence of the BH ejection. The outcome is an extended period of active star formation in the galaxy which yields a dense and massive nuclear stellar cusps. This type of nuclear regions could be a target property which would point out galaxies which underwent a BH ejection. Indeed, from an observational point of view, some galaxies have been tagged as candidates of having undergone a BH recoil (see eg. BCG in A2261 cluster (Postman et al. 2012), SDSS J1056+5516 (Kalfountzou et al. 2017), CID-42

(Civano et al. 2012), NGC 1399, 4261, 4486, IC 429 (Lena et al. 2014), 3C 186 radio quasar (Chiaberge et al. 2017) and Komossa (2012) for a review). On top of ejection via gravitational recoil, the complex dynamics of the two BHs before the final coalescence might cause the formation of a wandering black hole. If the two black holes spend enough time orbiting around each other (Begelman et al. 1980; Quinlan & Hernquist 1997) a third BH could reach their sphere of influence. As a consequence, the three BHs are likely to undergo a complex 3-body scattering interaction with the final outcome of the ejection of the less massive BH and the shrinking of the separation between the two remnants BHs (Volonteri et al. 2003; Volonteri & Perna 2005; Bonetti et al. 2019). Even though this type of interactions might not have a main role in the population of wandering black holes (see e.g. Volonteri et al. 2003; Volonteri & Perna 2005) they seem to play importance in speeding up the final BH-BH coalescence (Bonetti et al. 2018).

Wandering black holes can also be a consequence of the disruption of a satellite galaxy during the infall onto a larger system. Environmental processes such as ram pressure or tidal interactions, in fact, can gradually strip away satellites before they merge with the central galaxy (Moore et al. 1999; Springel et al. 2001). The frequency of satellite galaxy disruptions is still not well constrained. Some recent works have suggested that dwarf galaxies hosted in clusters are the ones which experience these events the most (Faltenbacher & Mathews 2005; Martel et al. 2012). Naively, the BHs hosted by the disrupted satellites are expected to be incorporated in the halo of the central galaxy and, thus, contribute to the population of wandering BHs. Even though such population of BHs is interesting because it would give an idea of the galaxy disruption rate, it has been mainly studied only through hydrodynamical simulations (Bellovary et al. 2010; Miki et al. 2014; Tremmel et al. 2018; Pfister et al. 2019). However, the current limits in the resolution achievable in simulations, make it difficult to well-resolve the fate of the cusp of stars and/or gas around the BH after the disruption and to properly assess the evolution of such “orphan” BHs.

Given the observational limitations in detecting wandering black holes, more theoretical work is needed to constrain where and how these black holes can be found with current and upcoming instruments. Several works have attempted to determine the orbits and time spent by a BH in a wandering orbit. For instance, by using 3D hydrodynamical simulation Blecha et al. (2011) found that at a fixed ratio between recoil and escape velocity, the recoil trajectories have a substantial variation with the galaxy gas fraction. On the other hand, under an analytic perspective, Choksi et al. (2017) explored different parameters and contributions in the orbital damping of wandering BHs finding a longer wandering phase in lighter halo and galaxy systems. These authors found that in many circumstances the wandering phase may be larger than the Hubble time.

In this work we use the L-Galaxies semi-analytical model in the version presented in Izquierdo-Villalba et al. (2019) to study the statistics and environment of black hole

growth and spin evolution and to explore the population of wandering black holes across cosmic time. We include both galaxy mergers and galaxy disk instabilities as physical processes that can lead to BH growth. For tracking spin evolution we follow the approach introduced by Sesana et al. (2014), where spin changes are coupled to the bulge assembly. We also introduce a time-delay between galaxy and BH mergers that depends on the BHs mass ratio and the galaxy gas fraction. Recoil velocities after BH coalescences are calculated on the basis of the progenitors properties while the trajectories of kicked BHs depend on the physical properties of the host halos and galaxies. We also follow the trajectory of *orphan* black holes from stripped satellites to complete the picture of wandering black holes.

The paper is organised as follows: in section 2 we describe the main characteristics of the semi-analytical model and the merger trees used in this work. In section 3 we describe all the physics included in the semi-analytical model to properly follow the BH mass growth, spin evolution and wandering phases. In section 4 we present our main findings regarding nuclear black holes (i.e., black holes in the center of galaxies). In section 5 we explore the properties of wandering black holes across cosmic time. In section 6 we present the effects of gravitational recoils in both BH occupation fraction and bulge-black hole mass relation. Finally, in section 7 we summarize our main findings. A Λ cold dark matter (Λ CDM) cosmology with parameters $\Omega_m = 0.315$, $\Omega_\Lambda = 0.685$, $\Omega_b = 0.045$, $\sigma_8 = 0.9$ and $H_0 = 67.3 \text{ km s}^{-1} \text{ Mpc}^{-1}$ is adopted throughout the paper (Planck Collaboration et al. 2014).

2 GALAXY FORMATION MODEL

In this section we briefly describe the L-Galaxies semi-analytical model (SAM) and the dark matter simulations used in this work. The bulk of the model is the one presented in Henriques et al. (2015), with the modifications detailed in Izquierdo-Villalba et al. (2019) which contribute to a better description of galaxy morphologies and radii for both the Millennium and MillenniumII merger trees.

2.1 Merger trees

The version of L-Galaxies used in this work is built on top of the subhalo merger trees of the Millennium (hereafter MS, Springel 2005) and Millennium II (hereafter MSII, Boylan-Kolchin et al. 2009) dark matter (DM) N -body simulations. While MS follows the cosmological evolution of 2160^3 DM particles with a mass of $8.6 \times 10^8 M_\odot/h$ within a periodic cube of $500 \text{ Mpc}/h$ on a side, MSII tracks the same number of particles in a box 125 times smaller in volume ($100 \text{ Mpc}/h$ on a side) but with 125 times better mass resolution ($6.885 \times 10^6 M_\odot/h$). Both simulations were run with GADGET code (Springel et al. 2001; Springel 2005) by using WMAP1 & 2dFGRS concordance cosmology: $\Omega_m = 0.25$, $\Omega_b = 0.045$, $\Omega_\Lambda = 0.75$, $h = 0.73 \text{ km s}^{-1} \text{ Mpc}^{-1}$, $n = 1$, $\sigma_8 = 0.9$ (Colless et al. 2001). However, the latest L-Galaxies version was tuned on a re-scaled versions of MS and MSII simulations (Angulo & White 2010) to match the

cosmological parameters obtained by Planck first-year data (Planck Collaboration et al. 2014): $\Omega_m = 0.315$, $\Omega_\Lambda = 0.685$, $\Omega_b = 0.045$, $\sigma_8 = 0.9$ and $h = 0.673 \text{ km s}^{-1} \text{ Mpc}^{-1}$.

Particle data of MS and MSII simulations were stored respectively at 63 and 68 epochs or *snapshots* spaced approximately logarithmically in time at $z > 0.7$ and linearly at $z < 0.7$ (see Boylan-Kolchin et al. 2009). Dark matter halos were selected within these snapshots by using a friend-of-friend (FOF) group-finder. Subhalos structures, i.e locally overdense, self-bound particle groups formed inside the DM halos, were identified with SUBFIND algorithm (Springel et al. 2001). By applying L-HALOTREE (Springel 2005) all halos and subhalos were arranged in merger trees structures allowing to follow the evolutionary path of any DM (sub)halo in the simulations. Although these (subhalo) merger trees structures are the skeleton of the SAM, the time resolution given by their 63 and 68 snapshots are not enough to properly trace the baryonic physics. Thus, to accurately follow the galaxy evolution, the SAM does an internal time discretization between two consecutive snapshots with approximately $\sim 5\text{--}20 \text{ Myr}$ of time resolution. These extra-temporal subdivisions used by the SAM are called *sub-steps*. Even though this work is based on the merger trees of the Millennium simulation, we combine them with the ones of Millennium II (as detailed in Section 2.2.3) to improve the galaxy and black hole initialization.

2.2 Baryonic physics

We briefly describe here the baryonic processes included in L-Galaxies that lead to the build up of the disk and bulge components.

2.2.1 Galaxy disk

In the current understanding of how cosmological structures form, it is accepted that the initial density fluctuations of the early universe act as the birthplaces of dark matter halos (Press & Schechter 1974). As soon gravitational instability triggers the collapse of these density fluctuations, part of the diffuse baryonic gas present in the universe is attracted and collapsed within them. Following this scenario, L-Galaxies starts associating a baryonic matter to each newly resolved DM subhalo in a form of diffuse, pristine, spherical and quasi-static *hot* gas atmosphere. Gradually, a fraction of this atmosphere is allowed to condensate and migrate towards the center of the subhalo, leading to the formation of a cold, rotationally supported gas component (White & Rees 1978). If the mass of the cold gas structure is large enough, star formation (SF) episodes are prompted, leading to the build-up of the stellar disk component. Shortly after the SF event, a fraction of the new stars explode as supernovae, enriching the environment with newly formed heavy elements, reheating a fraction of cold gas via energy injection and, eventually, expelling part of the hot gas atmosphere beyond the subhalo virial radius, R_{200c} (Guo et al. 2011). At later times, this ejected hot gas is allowed to be reincorporated into the gas atmosphere, being available once again for cooling onto the galactic disk. The reincorporation of this ejecta at later times helps to reg-

ulate the low- z star formation, especially in low-mass galaxies (Henriques et al. 2015). Besides, to prevent the stellar component of massive galaxies from overgrowth, the model introduces feedback from central supermassive black holes (BHs) as an additional mechanism to regulate star formation at low redshifts (see Section 3).

2.2.2 Galaxy bulge

Galaxies are allowed to assembly a bulge component via *galaxy mergers* and *disk instabilities*. While the former is related with the hierarchical growth of the DM subhalos, the latter takes more importance in isolated galaxies with a quiet merger history.

Galaxy encounters follow the merger of the two parent subhalos on a time-scale given by the dynamical friction presented in Binney & Tremaine (1987). According to the baryonic (gas plus stars) mass ratio of the two involved galaxies, m_R , the model differentiates between *major* ($m_R > m_R^{\text{th}}$) and *minor* ($m_R < m_R^{\text{th}}$) interactions (m_R^{th} is set to 0.2 as in Izquierdo-Villalba et al. 2019). Major interactions are assumed to completely destroy the disks of the two interacting galaxies, generating a pure spheroidal remnant which undergoes a *collisional starburst*. On the other hand, during minor interactions the disk of the larger galaxy survives and experiences a burst of star formation, while its bulge integrates the entire stellar mass of the satellite (see Guo et al. 2011). Besides, the model used in this work includes the prescription of *smooth accretion* in order to deal with the physics of extreme minor mergers (Izquierdo-Villalba et al. 2019). During those events it is expected that the stellar remnant of the satellite (bulge and disk) gets diluted inside the disk of the central galaxy before being able to reach the nucleus, thus, losing the possibility of make the bulge of the primary to grow.

On the other hand, in L-Galaxies a disk instability (DI) event refers to the process by which the stellar disk becomes massive enough to be inclined to non-axisymmetric instabilities which eventually lead to the formation of a central ellipsoidal component trough the buckling of nuclear stellar orbits (see references in Mo et al. 2010). During this process, the result is the formation of a *bar* and/or *pseudobulge* structure (Combes & Sanders 1981; Pfenniger & Norman 1990; Athanassoula 2005; Sellwood 2016; Spinoso et al. 2017). The L-Galaxies model accounts for galactic DI with an analytic stability criterion based on the Efstathiou et al. (1982) and Mo et al. (1998) simulations:

$$\frac{V_{\text{max}}}{(GM_{\star,d}/R_{\star,d})^{1/2}} \leq \epsilon^{\text{DI}}, \quad (1)$$

where V_{max} is the maximum circular velocity of the host dark matter, $R_{\star,d}$ and $M_{\star,d}$ are respectively the length and stellar mass of the stellar disk and ϵ^{DI} a parameter which determines the importance of the disk self-gravity (set to 1.5 as in Izquierdo-Villalba et al. 2019). If the stability criterion of Eq. (1) is met, an amount

$$\Delta M_{\text{stars}}^{\text{DI}} = M_{\star,d} - \left(V_{\text{max}}^2 R_{\star,d} / G \epsilon_{\text{DI}}^2 \right), \quad (2)$$

of the disk stellar mass is transferred to the bulge in order to

restore the disk (marginal) stability. Following the history and the physical conditions of the galaxy in which a DI takes place, the model distinguishes between instabilities that are *merger-induced* and the ones that are a consequence of the slow, *secular* evolution of galaxies. On one hand, *merger-induced* DIs are produced as a consequence of the fast increase of stellar disk mass after the collisional starburst or *smooth* satellite galaxy accretion. On the other hand, *secular* DIs result from the slow, but continuous, mass growth of the disk, taking a major importance in galaxies evolving in isolation. Under the assumption that bars and pseudobulges are a consequence of the secular evolution of galaxies (Debattista et al. 2006; Méndez-Abreu et al. 2010; Kormendy & Ho 2013; Moetazedian et al. 2017; Zana et al. 2018a,b; Rosas-Guevara et al. 2020) the model of Izquierdo-Villalba et al. (2019) links *secular* DIs with the formation of galactic bars and pseudobulges, whereas *merger-induced* DIs contribute to the formation of classical bulges. For more details we refer the reader to Izquierdo-Villalba et al. (2019).

Finally, in order to distinguish between bulge morphologies in the SAM, we follow the definition of Izquierdo-Villalba et al. (2019). In brief, we assume that a galaxy hosts a pseudobulge when the fraction of bulge formed via *secular induced* DI is at least 2/3. Galaxies display a classical bulge or elliptical structure when the fraction of bulge formed via *secular induced* DIs is smaller than 2/3 of the total bulge mass and its *bulge-to-total* stellar fraction (B/T) is respectively $0.01 < B/T < 0.7$ and $B/T > 0.7$. Finally, galaxies with $B/T < 0.01$ are considered bulgeless galaxies.

2.2.3 Improving the galaxy initialization in *Millennium trees*

As we discussed, the SAM populates each new resolved subhalo with an amount of hot gas in form of a diffuse atmosphere. From that moment, different analytical recipes are included to deal with the baryonic physical processes that lead to a mature galaxy. The subhalo mass resolution of the *Millennium* simulation used in this work ($M_{\text{halo}}^{\text{Res}} \sim 10^{10} M_{\odot}/h$) imposes a clear limit on the galaxy and BH evolutionary pathway that can be followed. Nevertheless, new resolved subhalos could already host a mature galaxy and its evolved BH. To improve this aspect we follow the approach of Bonoli et al. (2014) and Angulo et al. (2014) initializing each MS subhalo with random galaxies (hosted in the same redshift and subhalo mass) extracted from a run of *L-Galaxies* on top of the high resolution *Millennium* II merger trees ($M_{\text{halo}}^{\text{Res}} \sim 10^8 M_{\odot}/h$). The galaxy *grafting* includes all the properties of the galaxy and its respective central black hole (including wandering BHs). We stress that this does not imply for our model to be able to follow subhalos below the resolution limit of MS, as we do not have access to their merger history and cosmological evolution. The aim of this procedure is to better match the DM mass of the newly resolved subhalo to the properties of the newly initialised host galaxy.

3 A COMPREHENSIVE MODEL OF BLACK HOLE GROWTH

Astrophysical black holes can be fully determined by two quantities: *mass* and *spin*. In this section we present the implemented physic to track their evolution along the cosmic history.

3.1 Black hole seeding and spin initialization

Even though the existence of BHs is now well established, their origin is still an open issue. Up to date, several theories have been proposed and explored (see Volonteri 2010; Mayer & Bonoli 2019, for a review). The most studied one is the *light seed scenario* where BHs of mass between $10 - 100 M_{\odot}$ were formed at $z \gtrsim 20$ as remnants of Population III stars (Pop III, Madau & Rees 2001; Heger & Woosley 2002). Another complementary formation channel is the *heavy seed scenario* where much more massive black holes ($\sim 10^4 - 10^5 M_{\odot}$) are formed after the direct collapse of massive gas clouds, either in pristine primordial halos or in gas-rich merging galaxies (Koushiappas et al. 2004; Volonteri & Stark 2011; Mayer et al. 2010; Bonoli et al. 2014). In this work we simply assume that each newly resolved subhalo (independently of redshift and halo properties) is seeded with an initial BH mass of $10^4 M_{\odot}$. This initial seed mass is a reasonable assumption given the minimum mass of new resolved subhalos in MS and MSII ($\sim 10^{10} M_{\odot}$ and $\sim 10^8 M_{\odot}$, respectively). In future works, a proper BH seeding in *L-Galaxies* will be tackled (Spinoso et al. in prep.).

Besides the initial mass, the BH angular momentum, $|\vec{J}_{\text{BH}}|$, has to be set. The exact value of $|\vec{J}_{\text{BH}}|$ can be expressed as:

$$|\vec{J}_{\text{BH}}| = \frac{1}{\sqrt{2}} M_{\text{BH}} a (GM_{\text{BH}} R_{\text{Sch}})^{1/2} = \frac{a GM_{\text{BH}}^2}{c}, \quad (3)$$

where $R_{\text{Sch}} = 2GM_{\text{BH}}/c^2$ is the Schwarzschild radius, G the gravitational constant, c the light speed, and a the dimensionless *spin* parameter, whose value can be in the range $0 < |a| < 0.998$ (Thorne 1974). While M_{BH} and R_{Sch} are fully determined by the seed mass, the value of a does not have to depend on the initial mass. Indeed, no observational constraints and theoretical predictions about the initial BH spin exist to date (see e.g. Batta et al. 2017; Fuller & Ma 2019; Roulet & Zaldarriaga 2019; Zackay et al. 2019). Here we assume that the initial value of a is a random number selected between $0 < |a| < 0.998$. We have tested that the initial selection of a does not affect the results presented in this work. In fact, a BH loses any memory of its initial spin when it has accreted in a coherent way a gas mass comparable to its own (see for instance Fanidakis et al. 2011, Figure 1).

3.2 Black hole gas accretion

In this section we summarize the different mechanisms that feed central black holes with gas: (i) galaxy mergers, (ii) galaxy disk instabilities and, (iii) gas accretion from the hot gas atmosphere.

3.2.1 Cold phase accretion

The cold gas accretion is triggered by two different processes: galaxy mergers and disk instabilities.

i) *Gas accretion after mergers.* Simulations have shown that gravitational torques during galaxy mergers are able to drive cold gas towards the galaxy inner regions, triggering the black hole accretion (Di Matteo et al. 2005; Springel 2005; Hopkins et al. 2009). Following Kauffmann & Haehnelt (2000), Croton (2006) and Bonoli et al. (2009) we assume that the fraction of cold gas accreted by the BH after a galaxy merger is:

$$\Delta M_{\text{BH}}^{\text{gas}} = f_{\text{BH}}^{\text{merger}} (1 + z_{\text{merger}})^{3/2} \frac{m_{\text{R}}}{1 + (V_{\text{BH}}/V_{200\text{c}})^2} M_{\text{gas}}^{\text{Cold}}, \quad (4)$$

where $\Delta M_{\text{BH}}^{\text{gas}}$ includes a dependence on the galaxy baryonic merger ratio, $m_{\text{R}} < 1$, the virial velocity of the host DM subhalo, $V_{200\text{c}}$, the redshift of the merger, z_{merger} , and two adjustable parameters V_{BH} and $f_{\text{BH}}^{\text{merger}}$ set to 280 km/s and 0.034, respectively.

ii) *Gas accretion after disk instabilities.* Non-axisymmetric instabilities of galactic disks have a deep impact on the morphology of the nuclear parts. They are able to modify the gas disk structure via gravitational torques (see Shlosman & Begelman 1989; Hopkins & Quataert 2010). These processes produce strong gas inflows that lead to nuclear bursts of star formation and can drive part of the gas also in the BH surroundings (Shlosman et al. 1989; Hopkins et al. 2009; Hopkins & Quataert 2010; Fanali et al. 2015; Du et al. 2017; Spinoso et al. 2017). Consequently, each time a galaxy undergoes a disk instability episode we allow the central black hole to accrete an amount of gas given by:

$$\Delta M_{\text{BH}}^{\text{gas}} = f_{\text{BH}}^{\text{DI}} (1 + z_{\text{DI}})^{3/2} \frac{\Delta M_{\text{stars}}^{\text{DI}}}{1 + (V_{\text{BH}}/V_{200\text{c}})^2}, \quad (5)$$

where V_{BH} and $V_{200\text{c}}$ are the same parameters described before, z_{DI} the redshift in which the DI takes place and $\Delta M_{\text{stars}}^{\text{DI}}$ the mass of stars that triggers the stellar disk instability (see Eq. 2). $f_{\text{BH}}^{\text{DI}}$ is a free parameter that takes into account the gas accretion efficiency. As we discussed in Section 2.2.2, we assume DIs to be the consequence of either the galaxy secular evolution or of galaxy minor mergers. In the former case, we set the efficiency $f_{\text{BH}}^{\text{DI}} = 0.008$. Instead, for the case of merger-induced DIs, which are causally connected with the last galaxy minor interaction ($\lesssim 10 t_{\text{dyn}}^*$, Izquierdo-Villalba et al. 2019) we assume $f_{\text{BH}}^{\text{DI}} = f_{\text{BH}}^{\text{merger}}$, i.e. since the system is not relaxed the torque causing the gas inflow during the DI has the same efficiency that the one of the merger (Hopkins & Quataert 2010). The exact values of f_{BH} for both mergers and DI have been chosen to match the observed correlation between the bulge and the BH mass.

In this work, we assume that all the cold gas accreted by the BH after a merger or disk instability is stored in a reservoir, M_{res} . Motivated by numerical simulations, the reservoir is progressively consumed according to a *light curve* composed by two different phases (Hopkins et al. 2005, 2006a). While the first one is characterized by a rapid growth truncated at Eddington limit, the second one

is a quiescent regime of low accretion rates which starts when the BH reaches a certain threshold of accreted mass. Previous works have shown that this average AGN light curve is able to match successfully the faint end of the AGN luminosity functions (Marulli et al. 2008; Bonoli et al. 2009; Hirschmann et al. 2012; Volonteri et al. 2013). Note that if a galaxy undergoes a new merger or DI while the central BH is still accreting mass from a previous event, the new cold gas driven in the BH surroundings is added to the previous remnant gas reservoir and the light curve re-starts under the new initial conditions.

To characterize both phases we use the *Eddington factor*, f_{Edd} , defined as:

$$L_{\text{bol}}(t) = f_{\text{Edd}}(t) L_{\text{Edd}}(t), \quad (6)$$

where L_{bol} and L_{Edd} are respectively the black hole bolometric and Eddington luminosity. These quantities can be expressed as:

$$L_{\text{Edd}}(t) = \frac{4\pi G m_p c}{\sigma_{\text{T}}} \dot{M}_{\text{BH}}(t) = \frac{M_{\text{BH}}(t) c^2}{t_{\text{Edd}}}, \quad (7)$$

$$L_{\text{bol}}(t) = \frac{\epsilon(t)}{1 - \eta(t)} \dot{M}_{\text{BH}} c^2, \quad (8)$$

where σ_{T} is the Thomson scattering cross-section for the electron, m_p the proton mass, $t_{\text{Edd}} = \sigma_{\text{T}} c / (4\pi m_p G) = 0.45$ Gyr and η and ϵ the black hole accretion and radiative efficiency, respectively. Notice that, since we want to obtain a general equation that describes the growth of supermassive black holes, in Eq. (8) we have distinguished between η and ϵ . We refer to other works such as Pacucci & Ferrara (2015) or Volonteri et al. (2015) in which the same distinction is performed.

By definition of Eddington limit, the first phase is characterized by $f_{\text{Edd}}(t) = 1$. The BH grows in this phase for the time necessary to reach the mass $M_{\text{BH,peak}}$ defined by the moment in which the BH consumed a fraction γ (free parameter set to 0.7) of its whole gas mass reservoir (see Marulli et al. 2008; Bonoli et al. 2009; Hirschmann et al. 2012). Once this mass is reached, the black hole enters in a self-regulated or quiescent growth regimen characterized by small f_{Edd} values. Following Hopkins et al. (2006b) we assume that f_{Edd} in this phase is parametrized as:

$$f_{\text{Edd}}(t) = \frac{1}{[1 + (t/t_Q)^{1/2}]^{2/\beta}}, \quad (9)$$

where $t_Q = t_0 \xi^\beta / (\beta \ln 10)$, being $t_0 = 1.26 \times 10^8$ yr, $\beta = 0.4$ and $\xi = 0.3$ (see the discussion of these values in Hopkins et al. 2006b). We highlight that t is relative to the moment in which the BH finishes the Eddington phase.

As pointed out by Hopkins et al. (2006b) and Merloni & Heinz (2008) we also take into account the fact that the radiative efficiency has a dependence with the accretion efficiency and the nature of the accretion flow:

$$\epsilon(\eta, f_{\text{Edd}}) = \begin{cases} \eta & f_{\text{Edd}} > f_{\text{Edd}}^{\text{crit}} \\ \eta \left(\frac{f_{\text{Edd}}}{f_{\text{Edd}}^{\text{crit}}} \right) & f_{\text{Edd}} \leq f_{\text{Edd}}^{\text{crit}} \end{cases} \quad (10)$$

where $f_{\text{Edd}}^{\text{crit}}$ (Merloni & Heinz 2008; Volonteri et al. 2013, set to 0.03) is the *Eddington factor* by which below it the accretion disc becomes radiatively inefficient.

Finally, the black hole mass evolution during any accretion event can be obtained from the black hole growth rate, $\dot{M}_{\text{BH}} = dM_{\text{BH}}/dt$. By using Eq. (6), Eq. (7) and Eq. (8), \dot{M}_{BH} can be computed as:

$$\dot{M}_{\text{BH}} = f_{\text{Edd}}(t) \left(\frac{1 - \eta(t)}{\epsilon(t)} \right) \frac{M_{\text{BH}}(t)}{t_{\text{Edd}}}, \quad (11)$$

As we will see in Section 3.3, ϵ and η experience a time variation given their dependence with the black hole spin, a , which varies with time as a consequence of BH-BH mergers and gas accretion. In order to ease notation, instead of denoting the accretion and radiative efficiency as $\eta(a(t))$ and $\epsilon(a(t))$ we will use just the notation η and ϵ .

3.2.2 Hot phase accretion

This mechanism of black hole growth is triggered by the accretion of the hot gas which surrounds the galaxy. Following Henriques et al. (2015) the BH mass accretion rate during this mode is determined by:

$$\dot{M}_{\text{BH}} = k_{\text{AGN}} \left(\frac{M_{\text{hot}}}{10^{11} M_{\odot}} \right) \left(\frac{M_{\text{BH}}}{10^8 M_{\odot}} \right), \quad (12)$$

where M_{hot} the total mass of hot gas surrounding the galaxy and k_{AGN} is a free parameter set to $3.5 \times 10^{-3} M_{\odot}/\text{yr}$ to reproduce the turnover at the bright end of the galaxy luminosity function.

As pointed out by Marulli et al. (2008), the accretion rate of Eq. (12) is orders of magnitude below the BH Eddington limit. Therefore the contribution of this *radio mode* in the black hole mass growth is minimal. However, the AGN feedback generated during this phase is essential to inject enough energy into the galaxy hot atmosphere to decrease or even stop the gas cooling rate in the galaxy (Croton 2006; Bower et al. 2006).

3.3 Tracing the BH spin evolution

In this section we present the main equations implemented in *L-Galaxies* to properly follow the evolution of BH spin. Note that we have applied the spin model presented here to both modes of gas accretion (hot and cold). However, since the hot gas accretion is characterized by small values of f_{Edd} , we do not expect a large variation of the spin during these accretion events.

3.3.1 Spin evolution during gas accretion

During an accretion event, the gas settles in a disk which may not lie in the equatorial plane of the black hole. The disk could have a random orientation with an angular momentum \vec{J}_{d} , misaligned with respect to the one of the black hole \vec{J}_{BH} . When this misalignment happens, the rotating BH induces on the disk the so called *Lense-Thirring precession* (Bardeen & Petterson 1975a). For large-viscosity disks¹ this

misalignment configuration is unstable making the orbital plane of the inner parts of the disk align (*prograde* orbit) or counter-align (*retrograde* orbit) to the black hole angular momentum. This process is called *Bardeen-Petterson effect* (Bardeen & Petterson 1975b). The criterion of counter-alignment was established by King et al. (2005) and it takes into account the ratio between the black hole and disk angular momentum and the angle θ formed between them:

$$\cos \theta < - \frac{|\vec{J}_{\text{d}}|}{2|\vec{J}_{\text{BH}}|}. \quad (13)$$

Thus, for most of the accretion event, the inner part of the accretion disk is aligned if i) $|\vec{J}_{\text{d}}| > 2|\vec{J}_{\text{BH}}|$ or ii) $|\vec{J}_{\text{d}}| < 2|\vec{J}_{\text{BH}}|$ and $\theta < \pi/2$. On the contrary, when $|\vec{J}_{\text{d}}| < 2|\vec{J}_{\text{BH}}|$ and $\theta > \pi/2$, the (anti-)alignment depends if the ratio of $|\vec{J}_{\text{d}}|/2|\vec{J}_{\text{BH}}|$ is small enough with respect to exact value of $\cos \theta$.

We model this in our semi-analytical framework following the spin model presented in Dotti et al. (2013) and Sesana et al. (2014). The model assumes that the gas available during an accretion event (given by M_{BH} , see Section 3.2) is accreted in chunks of transient accretion disks limited by self-gravity, instead of being consumed in a single episode (King et al. 2008). In an α -disk the self-gravity radius, $R_{\text{disk}}^{\text{sg}}$, is determined by the distance to the BH at which the Toomre parameter Q is less than unity: $Q \sim c_s \Omega / \pi G \Sigma \lesssim 1$, where Ω is the Keplerian angular velocity, c_s sound speed and Σ the gas surface density. Thus, the value of $R_{\text{disk}}^{\text{sg}}$ is:

$$\frac{R_{\text{disk}}^{\text{sg}}}{R_{\text{Sch}}} \approx 10^5 f_{\text{Edd}}^{-22/45} \left(\frac{\alpha}{0.1} \right)^{28/45} \left(\frac{M_{\text{BH}}}{10^6 M_{\odot}} \right)^{-52/45} \left(\frac{\eta}{0.1} \right)^{22/45}, \quad (14)$$

where R_{Sch} is the Schwarzschild radius and α the radial shear viscosity parameter (set from hereafter to 0.1). Concerning the self-gravity mass, M^{sg} , the value is expressed as:

$$M^{\text{sg}} \approx 2 \times 10^4 f_{\text{Edd}}^{4/45} \left(\frac{\alpha}{0.1} \right)^{-1/45} \left(\frac{M_{\text{BH}}}{10^6 M_{\odot}} \right)^{34/45} M_{\odot}, \quad (15)$$

which was computed by solving the expression $M^{\text{sg}} = \int_0^{R_{\text{disk}}^{\text{sg}}} 2\pi \Sigma(R) R^2 dR$ with a surface density:

$$\Sigma(R) = 7 \times 10^7 f_{\text{Edd}}^{7/10} \left(\frac{\alpha}{0.1} \right)^{-4/5} \left(\frac{M_{\text{BH}}}{10^6 M_{\odot}} \right)^{19/20} \left(\frac{\eta}{0.1} \right)^{-7/10} \left(\frac{R}{R_{\text{Sch}}} \right)^{-3/4} \text{ g cm}^{-2}. \quad (16)$$

To avoid unrealistic accretion episodes, Dotti et al. (2013) set the maximum mass of the transient accretion disk to the minimum between M^{sg} and a fixed molecular cloud mass, M^{clld} , set in our case to $7 \times 10^3 M_{\odot}$. As pointed out by Sesana et al. (2014), fixing the value of M^{clld} is an idealized case, as molecular clouds might be characterized by a broad mass spectrum ($\lesssim 10^5 M_{\odot}$) eventually dependent on the host galaxy properties. However, since the cloud mass function is not trivial, we follow Dotti et al. (2013) keeping M^{clld} constant over the whole BH life. The continuous increase of the BH mass during accretion episodes with constant M^{clld} implies the formation of accretion disks which carry less angular momentum relative to the BH.

¹ This property is met in the α -disk model which describes the accretion disk around black holes (Shakura & Sunyaev 1973).

In this way, the larger is the BH mass, the larger is the number of retrograde accretions possible given that the condition $|\vec{J}_d|/2|\vec{J}_{\text{BH}}| < 1$ holds for a significant fraction of the duration of each accretion event. Typically, the number of retrograde accretions exceeds the prograde ones at $M_{\text{BH}} = 4 \times 10^5 (0.1 f_{\text{Edd}}/\eta)^{-2/27} (M^{\text{cld}}/10^4 M_{\odot})^{45/34} M_{\odot}$. For a given cloud mass, the radius of the accretion disk is ²:

$$\frac{R_{\text{disk}}^{\text{cld}}}{R_{\text{Sch}}} \approx 4 \times 10^4 f_{\text{Edd}}^{-14/25} \left(\frac{M_{\text{cloud}}}{10^4 M_{\odot}} \right)^{4/5} \left(\frac{\alpha}{0.1} \right)^{16/25} \left(\frac{M_{\text{BH}}}{10^6 M_{\odot}} \right)^{-44/25} \left(\frac{\eta}{0.1} \right)^{14/25}. \quad (17)$$

Each transient accretion disk has associated an angular momentum $|\vec{J}_d|$ determined by [Perego et al. \(2009\)](#):

$$|\vec{J}_d| = \frac{8}{21} \frac{R_d^{7/4} (GM_{\text{BH}})^{1/2}}{A_v} M_{\text{BH}}, \quad (18)$$

where

$$A_v = 9.14 \times 10^6 f_{\text{Edd}}^{3/10} \left(\frac{\alpha}{0.1} \right)^{4/5} \left(\frac{M_{\text{BH}}}{10^6 M_{\odot}} \right)^{1/20} \left(\frac{\eta}{0.1} \right)^{-3/10} \text{cm}^{5/4}/\text{s}, \quad (19)$$

and i) $R_d = R_{\text{disk}}^{\text{cld}}$ if $M^{\text{cloud}} < M^{\text{sg}}$ or ii) $R_d = R_{\text{disk}}^{\text{sg}}$ if $M^{\text{sg}} < M^{\text{cld}}$.

Therefore, the BH spin evolution during any gas accretion episode is followed by using Eq.(14)-(18) and checking Eq.(13). If $|\vec{J}_d| > 2|\vec{J}_{\text{BH}}|$, the fraction of transient disks consumed in a prograd accretion, n_{Pa} , is always equal to 1. On contrary, when $|\vec{J}_d| < 2|\vec{J}_{\text{BH}}|$ the scenario is more complex and the exact value of $\cos\theta$ is needed to check the (anti)alignment. To determine $\cos\theta$ in the regime of $|\vec{J}_d| < 2|\vec{J}_{\text{BH}}|$, previous works have assumed the *chaotic accretion* presented in [King et al. \(2005, 2008\)](#), consisting in choosing randomly the value of $\cos\theta$ ([Fanidakis et al. 2011](#); [Volonteri et al. 2013](#)). This selection gives the same probability of having an alignment and counter-alignment, i.e. $n_p \approx 0.5$ ([King et al. 2005](#)). Since the gas accretion in a counter-rotating orbit spins down the BH more efficiently than the spin-up due to a co-rotating accretion, the net result of the *chaotic scenario* is a low-spinning BH population with a typical a value oscillating around 0.2 (see [King et al. 2008](#); [Berti & Volonteri 2008](#)). Here, instead, following the approach of [Dotti et al. \(2013\)](#) and [Sesana et al. \(2014\)](#), we assume a much more general scenario, allowing an asymmetry in the n_{Pa} value. According to [Sesana et al. \(2014\)](#) the fraction of transient disks accreted in a prograde accretion when $|\vec{J}_d| < 2|\vec{J}_{\text{BH}}|$ is given by:

$$n_{Pa} = F + \frac{|\vec{J}_d|}{2|\vec{J}_{\text{BH}}|} (1 - F), \quad (20)$$

where F is an *isotropy parameter* which takes into account the fraction of accretion events with an initial angular momentum with $\theta < \pi/2^3$.

² The value of $R_{\text{disk}}^{\text{cld}}$ is computed by solving $M^{\text{cld}} = \int_0^{R_{\text{disk}}^{\text{cld}}} 2\pi\Sigma(R)R^2 dR$.

³ Notice that by fixing $F = 0.5$ the model presented here becomes the standard *chaotic scenario* of [King & Pringle \(2006\)](#).

The particular conditions of the gas inflow at subparsec scales that determine the value of F are still unknown. [Hopkins & Quataert \(2010\)](#), by analyzing nested hydrodynamical simulations, found out that the gas inflow at $\sim \text{pc}$ scales displays a correlation with the non-axisymmetric disturbances that act on galactic scales such as mergers or dynamical instabilities of self-gravitating disks. As discussed previously, [King & Pringle \(2007\)](#) suggested that a chaotic BH feeding at small scales ($F = 1/2$) would offer a promising explanation of the growth of the most BHs. However, the large level of anisotropy during the chaotic accretion leads to a population of low spinning BHs which makes it difficult to reconcile the model with observations. In this work, to obtain a better agreement with the spin observations, we relaxed the chaotic scenario by following the the *assumption* of [Sesana et al. \(2014\)](#) which links the value of F to the bulge morphology. With this connection we presume that the gas driven to circumnuclear scales retains certain memory of both the event which triggered its nuclear in-inflow and the bulge assembly (see the recent observational work of [Smethurst et al. \(2019\)](#) which would suggest this). Specifically, in [Sesana et al. \(2014\)](#) the exact value of F is associated to the ratio between the bulk rotation velocity of the bulge, v , and its velocity dispersion, σ . This ratio gives an idea of the coherence motion of the galactic bulge. If $v/\sigma > 1$ then $F = 1$, if $v/\sigma = 0$ then $F = 0.5$ and if $0 < v/\sigma < 1$ then $F = (1 + v/\sigma)/2$. Thus, bulges characterized by a large coherent motion (e.g. bars) feed the BHs with a larger number of transient chunks of co-rotating accretion disks than bulges dominated by velocity dispersion (e.g. ellipticals).

Since the exact value of v/σ is shaped by a complex galaxy dynamics which **L-Galaxies** does not address, we decide to take the v/σ values from the observed probability distribution function (PDF) of pseudobulges, classical bulges and ellipticals presented in Eq. 14-18 of [Sesana et al. \(2014\)](#). In brief, while elliptical structures have an asymptotic PDF around 0, classical bulges have a PDF centred at ~ 0.55 (see Eq.15 and 16 of [Sesana et al. 2014](#)). For pseudobulges, we follow the *hybrid* model of [Sesana et al. \(2014\)](#) assuming a log-normal PDF with 0.34 dex of standard deviation and an average value given by its Eq.14. Following [Izquierdo-Villalba et al. \(2019\)](#) we assume that in **L-Galaxies**, DI *secular* events build-up the pseudobulge/bar structure, minor mergers and DIs *merger-induced* assembly the classical bulge component, and major mergers shape an elliptical galaxy. Therefore, each time that a galaxy undergoes one of these events we extract a random number from its v/σ out-coming bulge PDF and we perform a mass-weighted average between that value and the one which characterizes the bulge at that moment. In the case of major mergers, we re-set the value of v/σ with a value randomly selected from the elliptical-bulge PDF. For the special case of *smooth accretion* events which bring gas onto the BH but do not build-up a bulge structure, we assume that the v/σ of the gas brought towards the BH surroundings is linked to the kinematics of the galaxy gaseous disk. For that, as we did with the pseudobulges, we assume a log-normal PDF with 0.34 dex of standard deviation and an average value given by Eq.14 of [Sesana et al. \(2014\)](#).

Following Thorne (1974) we can determine the evolution of the BH spin by:

$$\dot{a} = [L_{\text{ISCO}}(a) - 2aE_{\text{ISCO}}(a)] \left(\frac{\dot{M}_{\text{BH}}}{M_{\text{BH}}} \right), \quad (21)$$

where M_{BH} is the black hole mass, \dot{M}_{BH} the accretion rate onto the black hole and L_{ISCO} , E_{ISCO} quote respectively the specific angular momentum and energy in the *innermost stable circular orbit* (ISCO). Since an accretion event is composed by a fraction of n_{Pa} prograde and $(1-n_{Pa})$ retrograde orbits, Eq. (21) can be rewritten as (Sesana et al. 2014; Barausse 2012):

$$\dot{a} = \left[\left(n_{Pa} L_{\text{ISCO}}^{\text{pro}}(a) + (1-n_{Pa}) L_{\text{ISCO}}^{\text{retro}} \right) - 2a \left(n_{Pa} E_{\text{ISCO}}^{\text{pro}}(a) + (1-n_{Pa}) E_{\text{ISCO}}^{\text{retro}}(a) \right) \right] \frac{\dot{M}_{\text{BH}}}{M_{\text{BH}}}, \quad (22)$$

where $L_{\text{ISCO}}^{\text{pro}}$ ($L_{\text{ISCO}}^{\text{retro}}$) and $E_{\text{ISCO}}^{\text{pro}}$ ($E_{\text{ISCO}}^{\text{retro}}$) are, respectively, the specific angular momentum and energy in a prograde (retrograde) ISCO (Bardeen et al. 1972).

Finally, the accretion efficiency, η , it is computed as (Bardeen 1970):

$$\eta = 1 - E_{\text{ISCO}} = 1 - \sqrt{1 - \frac{2}{3} \frac{1}{r_{\text{ISCO}}}}, \quad (23)$$

where r_{ISCO} is the radius of the ISCO (in units of $R_{\text{Sch}}/2$) and its exact value depends in the spin value and the (anti)alignment of the transient accretion disk (Bardeen et al. 1972; Barausse et al. 2012):

$$r_{\text{ISCO}} = 3 + Z_2 \mp a\sqrt{(3 - Z_1)(3 + Z_1 + 2Z_2)}, \quad (24)$$

where the upper and lower sign refers respectively to a prograde and retrograde orbits and the vales of Z_1 and Z_2 are determined by:

$$Z_1 = 1 + (1 - a^2)^{1/3} \left[(1 + a)^{1/3} + (1 - a)^{1/3} \right], \quad (25)$$

$$Z_2 = \sqrt{3a^2 + Z_1^2},$$

Therefore, the final value of η after a fraction of prograde n_{Pa} and $(1-n_{Pa})$ of retrograde orbits is:

$$\eta(a_{\text{BH}}) = n_{Pa} \eta_{\text{pro}}(a) + (1 - n_{Pa}) \eta_{\text{retro}}(a), \quad (26)$$

where η_{pro} and η_{retro} are the values of accretion efficiency computed from Eq (23) assuming a r_{ISCO} radius in a prograde and retrograde orbit, respectively.

3.3.2 Spin evolution after a BH-BH coalescence

The last stage of a BH binary system is the coalescence. The final spin of the remnant BH is shaped by the initial spin configuration of its progenitors and their initial masses. In this work we follow the results of Barausse & Rezzolla (2009) which found that the spin modulus of the remnant black hole, $|a_f|$, is determined by:

$$|a_f| = \frac{1}{(1+q)^2} \left[|a_1^2| + |a_2^2| q^4 + 2|a_2||a_1|q^2 \cos \alpha + 2(|a_1|\cos \beta + |a_2|q^2 \cos \gamma)|\ell| + |\ell|^2 q^2 \right]^{1/2}, \quad (27)$$

with

$$|\ell| = 2\sqrt{3} + t_2 \nu + t_3 \nu^2 + \frac{s_4}{(1+q)^2} (|a_1|^2 + |a_2|^2 q^4 + 2|a_1||a_2|q^2 \cos \alpha) + \left(\frac{s_5 \nu + t_0 + 2}{1+q^2} \right) (|a_1|\cos \beta + |a_2|q^2 \cos \gamma), \quad (28)$$

where $q = M_{\text{BH},2}/M_{\text{BH},1} \leq 1$ is the binary mass ratio, $\nu = q/(1+q)^2$ the symmetric mass ratio, $|a_1|$ and $|a_2|$ are the initial spin magnitudes, α is the angle formed between the two spins and β , γ the angle formed between the spin (1 and 2) with the orbital angular momentum, respectively. The other parameters are set to the following values: $s_4 = 0.1229 \pm 0.0075$, $s_5 = 0.4537 \pm 0.1463$, $t_0 = -2.8904 \pm 0.0359$, $t_3 = 2.5763 \pm 0.4833$ and $t_2 = -3.51714 \pm 0.1208$ (Barausse & Rezzolla 2009; Barausse 2012).

Given that in the SAM we only track the evolution of the BH spin modulus we have to establish the direction between the two black hole spins and their directions with respect to the orbital angular momentum, i.e the values of α , β and γ of Eq.(27) and Eq.(28). To do that, we use the standard approach of dividing the BH-BH mergers in two types (Barausse 2012; Volonteri et al. 2013): *wet* and *dry*. While the former is characterized by $(M_{\text{Res},1} + M_{\text{Res},2}) > (M_{\text{BH},1} + M_{\text{BH},2})$, the latter is characterized by $(M_{\text{Res},1} + M_{\text{Res},2}) < (M_{\text{BH},1} + M_{\text{BH},2})$. In the case of wet mergers, it has been shown that the dissipative dynamics between black holes and the massive gas disc produces a torque with the effect of aligning both spins to the orbital angular momentum. However, Dotti et al. (2010) showed that this alignment is not perfect and there is a residual offset in the spin direction relative to the orbital angular momentum at the level of 10° . Therefore for the wet BH mergers we assume that $\cos \alpha$, $\cos \beta$ and $\cos \gamma$ are random numbers between $[\cos 0^\circ - \cos 10^\circ]$. For dry mergers, we assume random values of $\cos \alpha$, $\cos \beta$ and $\cos \gamma$.

3.4 Black hole coalescence

3.4.1 Black hole binaries: merger delay

In the standard *hierarchical* paradigm galaxies grow mainly through mergers with smaller or comparable mass companions (White & Rees 1978). This fact, together with recent observational results confirming the existence of BHs being hosted in the center of galaxies (Haehnelt & Rees 1993), suggest that binary BH (BBH) systems have been formed and merged during the whole lifetime of the universe. The evolutionary pathway of BBHs is described by three different stages (Begelman et al. 1980): i) an initial *pairing* phase in which dynamical friction exerted by the galaxy gas and stars drives both BHs individually to the nucleus of the merger remnant eventually forming a binary; ii) a following *hardening* phase in which the BBH orbital separation shrinks due to three-body slingshots and/or interaction with a massive gaseous disk; iii) a final *gravitational wave inspiral* phase which drives the binary to the final coalescence (see Colpi 2014, and references therein for a review). Building on this scenario, several studies have

tackled the evolution of BBHs (see for instance Quinlan & Hernquist 1997; Sesana 2013; Kelley et al. 2017a,b; Bonetti et al. 2018, 2019). On the semi-analytical modelling side, up to date, most of the studies presented in the literature have assumed an instantaneous coalescence right after a galaxy-galaxy merger (see the few exceptions of Volonteri et al. 2003; Tanaka & Haiman 2009; Antonini et al. 2015; Bonetti et al. 2019, 2018). This might be an acceptable assumption at high- z , where galaxy interactions are gas rich and dynamical friction can efficiently reduce the angular momentum of both BHs and speed up the hardening and final coalescence (Mayer 2013; del Valle et al. 2015). However, at low- z galaxies are generally poorer in gas and the timescales for merger can become very large.

In this work we relax the assumption of instantaneous BH-BH coalescence by allowing for a time delay between the galaxy merger and the BH binary final coalescence. Therefore, we introduce the possibility for galaxy-merger remnants of hosting a binary BH system for a given time interval $t_{\text{delay}}^{\text{BH}}$. Following the results of several dedicated hydrodynamical simulations (Callegari et al. 2011a,b; Fiacconi et al. 2013; Mayer 2013; del Valle et al. 2015), we implement a simple prescription to determine the lifetime of a BH binary system:

$$t_{\text{delay}}^{\text{BH}} \approx 0.01 \left(\frac{0.1}{q} \right) \left(\frac{0.3}{f_{\text{gas}}} \right) \mathcal{F}(e) \text{ Gyr}, \quad (29)$$

where q (< 1) is the mass ratio between the two BHs at the moment of the galaxy-galaxy merger, f_{gas} is the galaxy gas fraction, $\mathcal{F}(e)$ is a factor which takes into account the dependence of $t_{\text{delay}}^{\text{BH}}$ with the binary eccentricity e (for simplicity, we assume $\mathcal{F}(e) \approx 1$) and the 0.01 Gyr amplitude is based on the hydrodynamical simulations of Dotti et al. (2007), Fiacconi et al. (2013) and del Valle et al. (2015) who found that the BH separation in a binary system decays, typically, at parsecs scales in few Myrs. We clarify that the $t_{\text{delay}}^{\text{BH}}$ presented in Eq. 29 refers only to the time spent by the BBH system in the hardening and gravitational wave inspiral phase. This is counted starting from the galaxy merger time computed by the L-Galaxies, which marks the moment in which the two galactic nuclei merge. We have checked that the black hole mass function, spin distribution and BH-Bulge scaling relation presented in this work do no significantly change if we run the model with a delay $100 t_{\text{delay}}^{\text{BH}}$. Even though the hydrodynamical simulations of Escala et al. (2004, 2005), Dotti et al. (2007) and Cuadra et al. (2009) showed that dense gaseous regions are very effective in hardening BBHs, promoting their coalescence in less than $\lesssim 10^7$ yr, the dependence with the gas fraction might be much more complex. For instance, Tamburello et al. (2017) showed that the final BH-BH coalescence can be speeded-up or delayed depending on the clumpiness of the circumnuclear discs around the BHs. In a future work we plan to explore how different assumptions for the merger delays affect the global BH population.

We allow both BHs to accrete their respective gas reservoir carried before the merger while they are in a binary system. We also assume that any new amount of gas accreted after the galaxy merger (see Section 3.2.1) is

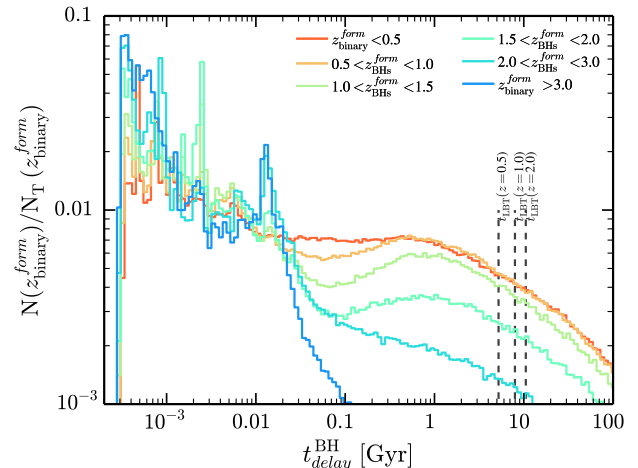


Figure 1. Distribution of BBH merger delay timescales, $t_{\text{delay}}^{\text{BH}}$, for different formation redshifts ($z_{\text{BHs}}^{\text{form}}$, as described in the legend). Vertical lines represents the lookback time (t_{LBT}) at $z=0.5, 1.0, 2.0$. Binary systems whose $z_{\text{BHs}}^{\text{form}}$ is 0.5, 1.0, 2.0 and are beyond these lines will not merge by $z=0$. The increase of the binary system lifetime towards low z is caused principally by the dependence of the gas fraction in Eq. (29).

added to the reservoir of the most massive BH. Still, the life of a galaxy is rather complicated and it can undergo multiple mergers in short time scales. If a merger happens in a moment in which the galaxy is still hosting a BBH, a third BH (or even another BBH) will perturb the system (Hut & Rees 1992). The final configuration is not trivial and few studies have addressed this (see e.g. Bonetti et al. 2019, 2018, and references therein). Here we use a simplified approach allowing only the two most massive BHs to remain in the galaxy (see Volonteri et al. 2003; Volonteri & Perna 2005). The lightest BH suffers a scattering event and it is ejected from the galactic nucleus. We highlight that we do not follow the wandering phase of these scattered BHs since we do not track the binary system separation (as, for instance, Volonteri et al. 2003 do) and therefore we cannot set the initial velocity of the ejection (see Section 3.5). We emphasize that our treatment of 3-body scattering is a simplified approach. Recent works of Hoffman & Loeb (2007) and Bonetti et al. (2018) pointed out that triple interaction can lead to the coalescence of stalled binaries. Even though this effect should be taken into account to have a complete picture of the evolution of BBHs, we do not expect significant modifications to our final results by neglecting it. For instance, Bonetti et al. (2018) found that triple interactions drive to coalescence *only* the $\sim 30\%$ of stalled binaries and, for those, the merger timescale is dictated by the dynamical friction timescale of the incoming intruder which is usually few hundreds of Myrs. In Appendix A the number density of both gravitational and 3-body scattering ejections is compared. We show that at any redshift and subhalo mass, the former is $\gtrsim 2$ dex more frequent. Finally, if the two initial BHs forming the binary system are the most massive ones, we eject the intruder without changing the $t_{\text{delay}}^{\text{BH}}$ value. Conversely, if there was an

exchange of BHs in the system, we reset the value of $t_{\text{delay}}^{\text{BH}}$ with the new initial conditions. The distribution of BH-BH merger delays, $t_{\text{delay}}^{\text{BH}}$, is presented in Fig. 1. As shown, the earlier is the redshift of binary formation, $z_{\text{BHs}}^{\text{form}}$, the shorter is the time spent by the two BHs in a binary system. While at $z_{\text{BHs}}^{\text{form}} > 3$ BBHs merge in $\lesssim 100$ Myr, at $z_{\text{BHs}}^{\text{form}} < 3$ a considerable fraction of BHs spend more than 1 Gyr orbiting each other before the final coalescence. Besides, at $z_{\text{BHs}}^{\text{form}} < 3$ a sizeable fraction of BBHs survive for times larger than the lookback time corresponding to their $z_{\text{BHs}}^{\text{form}}$, and therefore still inhabit galaxy nuclei today. The increase of the binary system lifetime towards low z is caused principally by the dependence of the gas fraction in Eq. (29). While at high- z galaxy mergers are mainly gas-rich, sinking effectively both BHs until the final coalescence, at low- z galaxies run out of gas stalling the two BHs in a binary system for a long time.

3.4.2 Final mass after a coalescence

Since gravitational waves carry away part of the energy of the system, the final mass of the remnant black hole, M_{BH}^{f} , is not the sum of the two progenitor black hole masses. According to Tichy & Marronetti (2008), the final mass of a black holes can be computed as:

$$M_{\text{BH}}^{\text{f}} = (M_{\text{BH},1} + M_{\text{BH},2}) [1 + 4\nu(m_0 - 1) + 16m_1\nu^2(a_1 \cos \beta + a_2 \cos \gamma)], \quad (30)$$

where $m_0 = 0.9515 \pm 0.001$, $m_1 = -0.013 \pm 0.007$.

3.5 The population of wandering black holes

Black holes outside of a galaxy in bound orbits within the dark matter halo are defined as wandering black holes (wBHs). In this section we study two types of events responsible for the formation of the wBH population: (i) *disruption of satellite galaxies* and (ii) *gravitational recoils* after a BH-BH merger.

3.5.1 Orphan black holes: a disruption event of its host galaxy

In **L-Galaxies**, as soon as two dark matter subhalos merge their host galaxies do it as well in a time scale given by the dynamical friction formula of Binney & Tremaine (1987). The smallest galaxy starts to sink towards the inner parts of its new host subhalo. During this process, if the galaxy is not compact enough it can be disrupted before reaching the subhalo center, losing the possibility to merge with the central galaxy. When this happens, the central black hole (or binary system) of the satellite galaxy is deprived of its host and is incorporated in the dark matter subhalo as a wBH. The disruption process implemented in **L-Galaxies** is presented in Guo et al. (2011). We follow the 3D orbit of the black hole using the formalism presented in Section 3.5.3. As initial conditions, we consider the position in which the satellite galaxy is disrupted ($\vec{p}_{\text{Sat}} = (x_{\text{Sat}}, y_{\text{Sat}}, z_{\text{Sat}})$) and the satellite galaxy velocity ($\vec{v}_{\text{Sat}} = (v_{\text{Sat}}^x, v_{\text{Sat}}^y, v_{\text{Sat}}^z)$) evaluated at

the same instant. Additionally, we assume that the black hole completely loses its accretion disk. From here onwards, we tag this type of wBHs as *orphan black holes*. In the upper panel of Fig. 2 we present a cartoon showing the formation of the orphan black hole population.

3.5.2 Ejected black holes: Kicks due to gravitational recoils

During a BH merger, the binary system emits gravitational waves able to carry away energy and angular momentum. Due to conservation of linear momentum, in the instant of the merger, the emission of gravitational waves imparts a kick to the remnant black hole. The velocity characterizing this kick is called *recoil velocity*, \vec{V}_{recoil} . Using numerical simulations of general relativity, it has been shown that recoil velocities can take a wide range of values: from small ones which just displace the remnant BH from the galaxy center, to larger values big enough to exceed the escape velocity of the host galaxy or even of the host halo (Baker et al. 2008; Lousto & Zlochower 2008; van Meter et al. 2010). Here we use the fitting formula established by Lousto et al. (2012):

$$\begin{aligned} \vec{V}_{\text{recoil}} &= v_m \hat{e}_1 + v_{\perp} (\cos \zeta \hat{e}_1 + \sin \zeta \hat{e}_2) + v_{\parallel} \hat{n}_{\parallel}, \\ v_m &= A_m \nu^2 \frac{(1-q)}{(1+q)} [1 + B_m \nu], \\ v_{\perp} &= H \frac{\nu^2}{(1+q)} (a_2^{\parallel} - q a_1^{\parallel}), \\ v_{\parallel} &= \frac{16\nu^2}{(1+q)} [V_{1,1} + V_A \delta_{\parallel} + V_B \delta_{\parallel}^2 + V_C \delta_{\parallel}^3] |\vec{a}_2^{\perp} - q \vec{a}_1^{\perp}| \cos(\phi_{\Delta} - \phi_1), \end{aligned} \quad (31)$$

where, v_m is the velocity due to the *mass-asymmetry contribution*⁴ and, v_{\parallel} , v_{\perp} are *spin contribution* producing kicks parallel and perpendicular to the orbital angular momentum respectively. As in the previous section, $q = M_{\text{BH}}^2 / M_{\text{BH}}^1 \leq 1$ is the binary mass ratio, $\nu = q/(1+q)^2$ the symmetric mass ratio, $|a_i|$ is the initial spin magnitude of the black hole i , \parallel and \perp refer respectively to components parallel and perpendicular to the orbital angular momentum. \hat{e}_1 and \hat{e}_2 are orthogonal unit vectors in the orbital plane. $\zeta = 145^\circ$ is the angle between the unequal mass and spin contribution (González et al. 2007; Lousto & Zlochower 2008), $\vec{S} = 2(\vec{a}_2 + q^2 \vec{a}_1)/(1+q)^2$. ϕ_{Δ} is the angle between the in-plane component $\vec{\Delta}^{\perp} = (M_{\text{BH}}^1 + M_{\text{BH}}^2)(\vec{S}_2^{\perp}/M_{\text{BH}}^2 - \vec{S}_1^{\perp}/M_{\text{BH}}^1)$ and the infall direction at merger. The values of the other coefficients are obtained numerically: $A_m = 1.2 \times 10^4$, $B_m = -0.93$, $H = 6.9 \times 10^3$ (González et al. 2007; Lousto & Zlochower 2008) and $V_{1,1} = 3677.76$ km/s, $V_A = 2481.21$ km/s, $V_B = 1792.45$ km/s and $V_C = 1506.52$ km/s (Lousto et al. 2012).

If the modulus of this velocity is larger than the escape velocity of its host galaxy, the black hole is kicked from it and incorporated in the DM halo as a wBH. Indeed, if the recoil velocity is large enough, the BH can even escape from the halo. This happens more frequently at high- z , where the halos are smaller and their potential wells shallower. This scenario is summarized in the lower cartoon displayed

⁴ since it does not depend on the spin it disappears in equal binary mass mergers

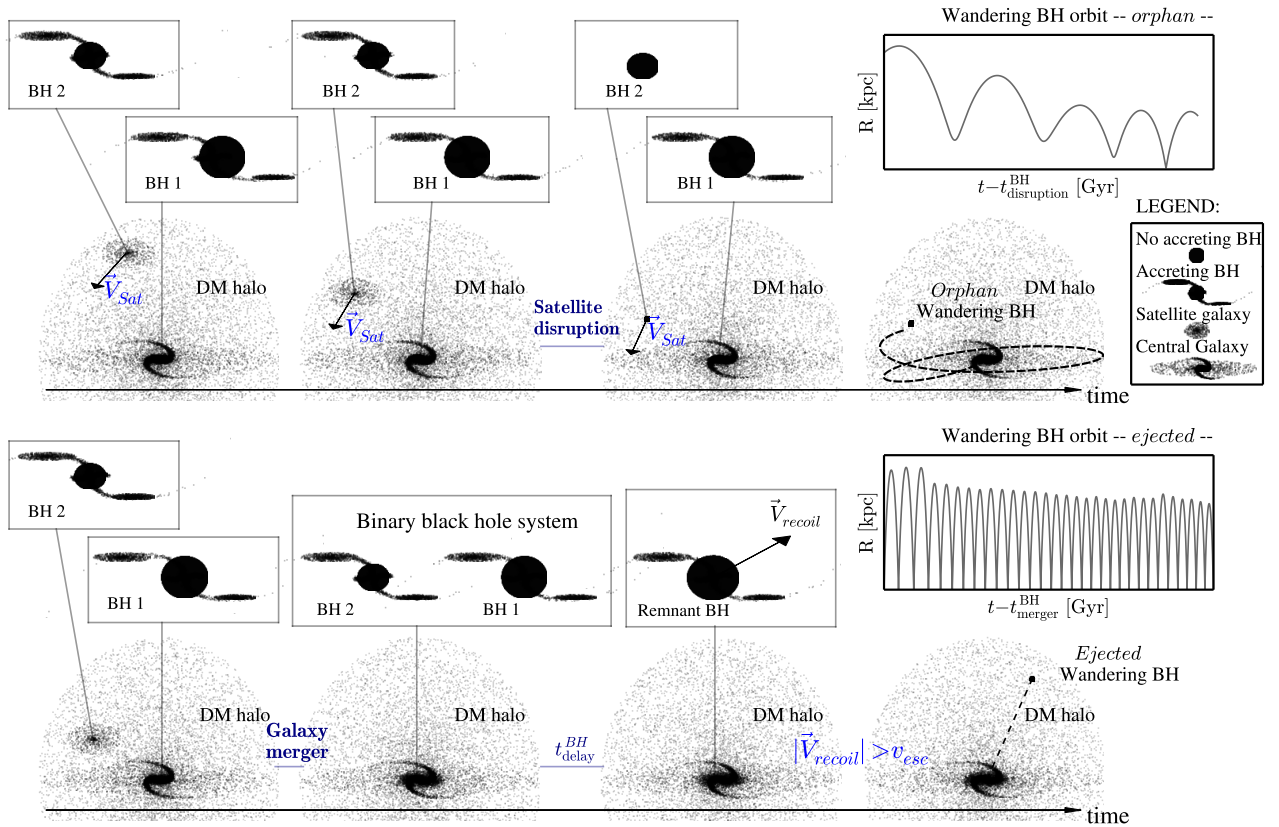


Figure 2. A schematic view of the two pathways that lead to wandering BHs. **Upper panel:** *Orphan* wandering black holes originate from the complete disruption of the host galaxy during its infall towards the central galaxy. Once the black hole is deprived of its host galaxy, we assume that its accretion disk (in case it was in an accreting phase), is also removed. The initial orbital speed of the new wandering BH is assumed to be the 3D velocity of the satellite galaxy at the disruption time \vec{V}_{Sat} (see Section 3.5.1). We highlight that an accreting BH is presented surrounded by a warped accretion disk. This is the result of the Bardeen-Petterson effect which makes the orbital plane of the inner parts of the disk align or counter-align to the black hole angular momentum. **Lower panel:** An *ejected* black hole is the result of the coalescence of a binary system (after a $t_{\text{delay}}^{\text{BH}}$ subsequent to the merger of the two host galaxies) and the resulting gravitational recoil. The kick velocity, \vec{V}_{recoil} , depends on the properties of two progenitors. If the modulus of the recoil velocity is larger than the escape velocity of the galaxy (v_{esc}) the kicked BH is ejected from the host galaxy, starting its wandering phase.

in Fig.2. Hereafter, we call this type of wBHs *ejected black holes*. When an *ejected* wBH is kicked out of its host galaxy we assume a *purely* radial motion for the orbital integration (i.e. along the \hat{r} coordinate without movement in the $\hat{\theta}$ and $\hat{\phi}$ ones, see Section 3.5.3). However, when an *ejected* wBH loses its host halo and is incorporated to a larger structure, after a galaxy merger, we start treating the *ejected* wBH as an *orphan* wBH, and we start tracking its 3D orbit according to the formalism presented in Section 3.5.5. In what follows, we will call *inborn* the *ejected* wBHs that are still orbiting the galaxy from whose nucleus they were ejected, while we will use the term *acquired* to refer to *ejected* wBHs that have lost their host galaxy and have been incorporated by the halo of a larger one.

Finally, we neglect the fact that the ejected BH can retain an accretion disk. It is not clear how massive is the disk that can be retained and subsequently accreted by a BH after a recoil (see Blecha et al. 2011). Loeb (2007) showed that in an α -disk the maximum amount of the disk material that a recoiled BH can carry out is, at most $\sim M_{\text{BH}}$ which accounts for a relatively small AGN lifetime

($\sim 4.5 \times 10^6 f_{\text{Edd}} / \epsilon \text{ yr}$, Volonteri & Madau 2008). In this work we neglect the accretion disk of ejected BHs, but we plan to include it in a future work, focused on the observability of AGN pairs.

3.5.3 Tracking the orbits of wandering black holes

Once in the wandering phase, the BH starts to orbit within the subhalo potential (i.e. around its centre r_0 ⁵). The equation of motion can be expressed as:

$$\ddot{\mathbf{u}} = \left(-\frac{\text{GM}(<(r-r_0))}{(r-r_0)^2} + a_{\text{df}}^{\text{cless}} + a_{\text{df}}^{\text{gas}} \right) \hat{\mathbf{u}}, \quad (32)$$

where the first term refers to the gravity acceleration caused by a mass $M(<(r-r_0))$ of dark matter, stars and gas (in both galaxy and inter-cluster medium) within a radius $r-r_0$. The second and third terms are related to

⁵ Here we assume that the galaxy position is always at the center of the host subhalo, i.e r_0

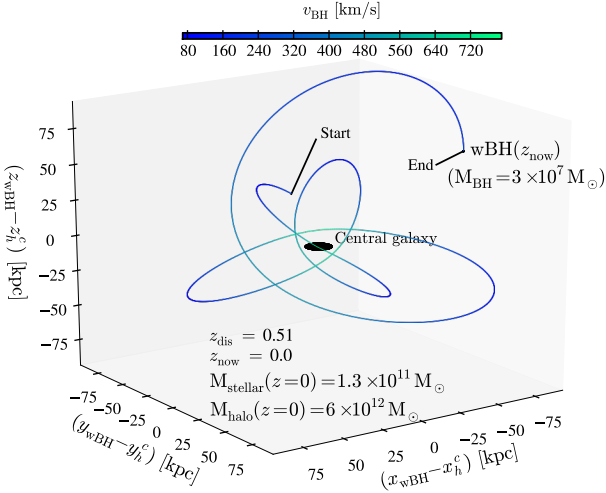


Figure 3. Orphan wBHs orbit extracted from L-Galaxies run on top of MS subhalo merger trees. The example presents a $\sim 10^7 M_{\odot}$ wBH formed at $z_{\text{dis}} = 0.51$ after the disruption of its host galaxy. The final ($z_{\text{now}} = 0$) halo and stellar mass of its central galaxy is $6 \times 10^{12} M_{\odot}$ and $1.3 \times 10^{11} M_{\odot}$, respectively. The color of the orbit encodes the modulus of the wBH velocity (v_{BH}).

the dynamical friction caused by collisionless (stars and dark matter) and gas components, respectively. Since in this work we are interested in the position of wBHs, we track their orbital evolution by solving numerically Eq. (32) using a 4th order *Runge-Kutta* integrator with time step of 1 Myr⁶. We have also used integration intervals of 0.1 Myr, obtaining nearly identical results.

Assuming a Maxwellian velocity distribution and a black hole velocity v_{BH} , the value of $a_{\text{df}}^{\text{class}}$ is determined by (Chandrasekhar 1943):

$$\tilde{a}_{\text{df}}^{\text{class}} = -\frac{4\pi G^2 M_{\text{BH}} \rho(r-r_0) \ln \Lambda}{v_{\text{BH}}^3} \left[\text{erf}f(\Gamma) - \frac{2\Gamma}{\sqrt{\pi}} e^{-\Gamma^2} \right] \hat{v}, \quad (33)$$

with $\Gamma = |v_{\text{BH}}|/\sqrt{2}\sigma$ where σ is the dark matter velocity dispersion computed as $\sigma = (GM_{\text{halo}}/2R_{200})^{1/2}$, $\text{erf}f$ is the error function and $\ln \Lambda$ is the Coulomb logarithm fixed to 3.1 (Escala et al. 2004; Gualandris & Merritt 2008; Blecha & Loeb 2008a). Finally, $\rho(r-r_0)$ is the mass density of the collisionless system enclosed within $r-r_0$. In our case $\rho(r-r_0) = \rho_{\text{DM}}(r-r_0) + \rho_{\text{ICM}}(r-r_0)$, i.e. the mass of dark matter and the mass of stars in the inter-cluster medium (ICM or stellar halo). For the case of dark matter we assume a NFW profile (Navarro et al. 1996)⁷ while for ICM an isothermal one.

Since galaxies are surrounded by hot gas which fills their host DM subhalos, we also take into account the dynamical friction caused by that gas. Escala et al. (2004) determined

that the damping of the oscillation amplitude for an object moving inside a gas follows the equation:

$$\tilde{a}_{\text{df}}^{\text{gas}} = -\frac{4\pi G^2 M_{\text{BH}} \rho_{\text{gas}}(r-r_0)}{v_{\text{BH}}^3} f(\mathcal{M}) \hat{v}, \quad (34)$$

where $\rho_{\text{gas}}(r-r_0)$ is the mass density of the hot gas at position $r-r_0$, $\ln \Lambda$ is again the Coulomb logarithm fixed to 3.1 and, \mathcal{M} the Mach number equal to $|v_{\text{BH}}|/c_s$ with c_s the sound speed computed as in Tanaka & Haiman (2009) and Choksi et al. (2017): $c_s \approx 1.8(1+z)^{1/2}(M_{\text{halo}}/10^7 M_{\odot})^{1/3}(\Omega_M h^2/0.14)$ km/s. The exact value of $f(\mathcal{M})$ is determined by:

$$f(\mathcal{M}) = \begin{cases} \frac{1}{2} \ln \Lambda \left[\text{erf}f\left(\frac{\mathcal{M}}{\sqrt{2}}\right) - \sqrt{\frac{2}{\pi}} \mathcal{M} e^{-\mathcal{M}^2/2} \right] & \text{if } \mathcal{M} \leq 0.8 \\ \frac{3}{2} \ln \Lambda \left[\text{erf}f\left(\frac{\mathcal{M}}{\sqrt{2}}\right) - \sqrt{\frac{2}{\pi}} \mathcal{M} e^{-\mathcal{M}^2/2} \right] & \text{if } 0.8 \leq \mathcal{M} \leq 1.5 \\ \frac{1}{2} \ln(1 - \mathcal{M}^{-2}) + \ln \Lambda & \text{if } \mathcal{M} > 1.5 \end{cases} \quad (35)$$

The integration of the wBH orbit stops when i) the black hole is re-incorporated in the galaxy (see Section 3.5.4), ii) the recoil velocity of ejected BHs is larger than the subhalo escape velocity or iii) the black hole position exceed $3 \times R_{200}$ (R_{200} is the subhalo virial radius) and it is still moving away from the galaxy.

As an example, in Figure 3 we present orbit evolution of an orphan wBHs extracted from L-Galaxies run on the MS subhalo merger trees. In particular, the wBH has a mass of $\sim 10^7 M_{\odot}$ and it was formed at $z \sim 0.5$ inside of a $\sim 10^{12} M_{\odot}$ subhalo.

3.5.4 Reincorporation of wBHs

We assume that a BH is reincorporated in a galaxy when it passes through the galaxy, $r < R_{\text{gal}}$ ⁸, with a velocity (v_{BH}) smaller than the galaxy escape velocity (v_{esc}), i.e. $v_{\text{BH}} < v_{\text{esc}}$. The exact value of v_{esc} is computed taking into account both bulge and disk (stellar and cold gas):

$$v_{\text{esc}} = \sqrt{v_{\text{esc,Bulge}}^2 + v_{\text{esc,Stellar disk}}^2 + v_{\text{esc,Cold disk}}^2}, \quad (36)$$

In the case of the bulge component we assume a Hernquist profile (Hernquist 1990) with an escape velocity at r_0 :

$$v_{\text{esc,Bulge}}^2 = 2 \left(1 + \sqrt{2} \right) \frac{G M_{\text{Bulge}}}{r_{\text{bulge}}}, \quad (37)$$

where M_{Bulge} is the total bulge mass and r_{bulge} the bulge half-mass radius. Although, this profile can approximate classical bulges, it is a rough approximation for pseudobulges.

⁶ Note that the *sub-steps* that L-Galaxies does between DM snapshots are $\sim 2-20$ Myr, depending on redshift

⁷ The concentration parameter as a function of redshift and subhalo mass has been computed by using the fits of Dutton & Macciò (2014).

⁸ R_{gal} is the galaxy radius computed as the mass weighted average between the bulge, stellar disk and cold gas disk. In Izquierdo-Villalba et al. (2019) we showed that the SAM, after including gas dissipation losses during the bulge size computation, is able to reproduce the galaxy radius of early and late type galaxies.

For stellar and cold gas disk we assume an exponential profile. In this case, the escape velocity at r_0 is determined by:

$$v_{\text{esc,Stellar/Cold disk}}^2 = 3.36 \frac{G M_{\text{Disk}}}{r_{\text{disk}}}, \quad (38)$$

where M_{Disk} is the total stellar/cold gas disk mass and r_{disk} its half-mass radius.

3.5.5 Changing reference system during merger events

The scenario described above complicates when galaxies merge. During the interaction, the satellite galaxy is first of all deprived of its host DM subhalo. In the following, we will refer to the ‘‘subhalo merger time’’ as the instant in which the satellite halo is no more identified within the underlying merger tree. Any wBHs which was hosted by the satellite galaxy now starts to be influenced by the potential of the larger central galaxy⁹. To track the new orbit, the position and velocity of the recently accreted wBHs, we need to change the reference system, so that the center is given by the new central galaxy position and velocity¹⁰:

$$\begin{aligned} x_{\text{wBH}}^{\text{new}} &= (x_h^s + x_{\text{wBH}}^s) - x_h^c; & v_{\text{wBH}}^{x,\text{new}} &= (v_h^{s,x} + v_{\text{wBH}}^x) - v_h^{c,x}, \\ y_{\text{wBH}}^{\text{new}} &= (y_h^s + y_{\text{wBH}}^s) - y_h^c; & v_{\text{wBH}}^{y,\text{new}} &= (v_h^{s,y} + v_{\text{wBH}}^y) - v_h^{c,y}, \\ z_{\text{wBH}}^{\text{new}} &= (z_h^s + z_{\text{wBH}}^s) - z_h^c; & v_{\text{wBH}}^{z,\text{new}} &= (v_h^{s,z} + v_{\text{wBH}}^z) - v_h^{c,z}, \end{aligned} \quad (39)$$

where (x_h^s, y_h^s, z_h^s) and $(v_h^{s,x}, v_h^{s,y}, v_h^{s,z})$ are, respectively, the positions and velocity of the satellite subhalo at the moment of merger. $[(x_h^c, y_h^c, z_h^c), (v_h^{c,x}, v_h^{c,y}, v_h^{c,z})]$ and $[(x_{\text{wBH}}, y_{\text{wBH}}, z_{\text{wBH}}), (v_{\text{wBH}}^x, v_{\text{wBH}}^y, v_{\text{wBH}}^z)]$ represent the same as before but for the central subhalo and wandering BH, respectively.

Although obtaining the exact value of $(x_{\text{wBH}}, y_{\text{wBH}}, z_{\text{wBH}})$ and $(v_{\text{wBH}}^x, v_{\text{wBH}}^y, v_{\text{wBH}}^z)$ for *orphan* (or *acquired ejected*) wBHs at the moment of the merger is simple because we follow their full 3D orbit, for *inborn ejected* wBHs is not trivial since we only follow their radial coordinate (see Section 3.5.2). In this case, we assume that they start the new orbit from a random location (in θ, φ) in a sphere of radius r . Once r, θ and φ are fixed, the Cartesian coordinates and velocities of the *inborn ejected* wBHs are determined by:

$$\begin{aligned} x_{\text{wBH}} &= |r| \sin \theta \cos \varphi; & v_{\text{wBH}}^x &= |v_{\text{BH}}| \sin \theta \cos \varphi, \\ y_{\text{wBH}} &= |r| \sin \theta \sin \varphi; & v_{\text{wBH}}^y &= |v_{\text{BH}}| \sin \theta \sin \varphi, \\ z_{\text{wBH}} &= |r| \cos \theta; & v_{\text{wBH}}^z &= |v_{\text{BH}}| \cos \theta. \end{aligned} \quad (40)$$

where r and v_{BH} are respectively the radial position and radial velocity of the *ejected* wBH at the moment of the halo merger.

⁹ The orbits of the wBHs moving around the central subhalo (galaxy) are also affected by the change of the dark matter potential as the differential equation which determines the orbit evolution depends on the halo mass at $r < r_{\text{wBH}}$, see Eq (32).

¹⁰ Notice that we assume that the galaxy position is always at the center of the host subhalo.

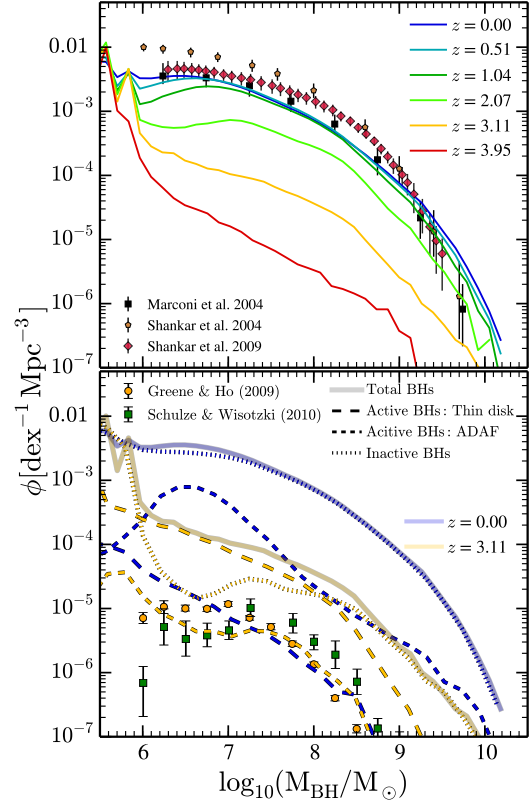


Figure 4. Upper panel: Redshift evolution of the black hole mass function compared to the observational results of Marconi et al. (2004) and Shankar et al. (2004, 2009). Lower panel: Black hole mass function at $z \sim 0$ and 3 (thick blue and yellow lines, respectively) divided between inactive ($f_{\text{Edd}} < 10^{-4}$, dotted lines) and active ($f_{\text{Edd}} > 10^{-4}$) black holes, where the latter are split in BHs accreting in the thin disk ($f_{\text{Edd}} > f_{\text{Edd}}^{\text{crit}}$, dashed lines) and ADAF ($10^{-4} < f_{\text{Edd}} < f_{\text{Edd}}^{\text{crit}}$, short dashed lines) phase. The black hole mass function of active BHs at $z \sim 0$ from Greene & Ho (2007) and Schulze & Wisotzki (2010) are added for comparison.

4 NUCLEAR BLACK HOLES

In this section we compare the predictions for nuclear black holes (i.e BHs located at the center of the host galaxy at the analyzed redshift) with a variety of available observational results. By checking the black hole mass function, the bolometric luminosity functions and spin values we prove that our black holes form a reliable population at $z \leq 4$. We do not present results beyond $z = 4$ since the model predictions are very sensitive to the exact seed mass assumed. In a future work, where a more careful seeding in L-Galaxies is modeled, we will analyze the high- z black hole population (Spinoso et al. in prep.). On top of this, we show only the results for BHs whose mass is larger than $10^6 M_{\odot}$, as at smaller masses the resolution of Millenium DM simulation does not allow us to draw reliable conclusions.

4.1 Black hole mass assembly

The evolution of the black hole mass function (BHMF) between $z = 0$ and $z = 4$ is shown in the upper panel of Fig. 4. There is a significant evolution from $z \sim 4$ up to $z \sim 2$, where the BHMF amplitude increases up to 2 dex. Conversely, at

$z < 1$ the BHMF does not evolve significantly. Such small evolution at low z indicates that most of the local BHs were already assembled by $z \sim 1$. Similar behavior is found in the theoretical work of Merloni & Heinz (2008) where a very weak evolution in the BHMF is seen below $z \sim 1$ and, as we find here, most of it happens at small masses ($< 10^7 M_\odot$). On the semi-analytical side, works such as Fanidakis et al. (2011); Griffin et al. (2019) or Marshall et al. (2020) show a stronger redshift evolution at $z \lesssim 1$ where the normalization of the BHMF increases relatively fast at $> 10^8 M_\odot$ and decreases at $\lesssim 10^8 M_\odot$. On the other hand, the results of Hirschmann et al. (2012) show a similar weak evolution in the BHMF at $z \sim 1$. In the same figure, we have compared the predictions at $z=0$ with the observational constraints provided by Marconi et al. (2004) and Shankar et al. (2004, 2009). Even though the BHMF of the model is compatible with the observations, mainly with Marconi et al. (2004), it displays a smaller amplitude when compared with Shankar et al. (2004, 2009). As pointed out by Shankar et al. (2016), this discrepancy might be caused by biases effects affecting the observations. Shankar et al. (2016) showed that, because of selection effects¹¹, the normalization of the scaling relations used to link the BH mass with galaxy properties (bulge velocity dispersion, total stellar mass and bulge mass) is increased by a factor $\gtrsim 3$ (see also Bernardi et al. 2007; Shankar et al. 2019). The lower amplitude in the empirical relations pointed out by Shankar et al. (2019) yields smaller BH masses, lower black hole mass density and higher radiative efficiencies which would support rapidly spinning BHs and lower levels of gravitational wave emission, consistent with the current non-detection of this signal by pulsar timing array experiments (see Sesana et al. 2016).

The lower panel of Fig.4 presents the BHMF of *active* and *inactive* BHs at $z \sim 0$ and 3. We consider as threshold between active and non-active the Eddington ratio $f_{\text{Edd}} \sim 10^{-4}$ (Rosas-Guevara et al. 2016), i.e below this value the emission of the BH is essentially undetectable against the emission of the host galaxy. Even though this threshold is quite arbitrary, we did not find significant differences in the results assuming a threshold between $10^{-3} - 10^{-5}$. The inactive population increases from $z \sim 3$ to $z \sim 0$, with the most massive BHs becoming non-active at an earlier epoch: while at $z \sim 3$ inactive BHs have typical $M_{\text{BH}} > 10^8 M_\odot$, at $z \sim 0$, black holes with masses $M_{\text{BH}} > 10^6 M_\odot$ are inactive. This behaviour is usually referred to as *downsizing*, and it has been reported by observational works (Merloni et al. 2004; Heavens et al. 2004; Hasinger et al. 2005), semi-analytical models (Bonoli et al. 2009; Fanidakis et al. 2012; Hirschmann et al. 2012) and cosmological hydro-simulations (Sijacki et al. 2009; Rosas-Guevara et al. 2016; Thomas et al. 2019). In the same figure we divided the active population by accretion geometry. We assume that the emission of active BHs with $f_{\text{Edd}} > f_{\text{Edd}}^{\text{crit}}$ can be described by the thin and radiatively-efficient Shakura-

Sunyaev disk model (Shakura & Sunyaev 1973, *thin disk geometry*, hereafter). On the other hand, the emission of active BHs with $10^{-4} < f_{\text{Edd}} < f_{\text{Edd}}^{\text{crit}}$ are associated to a thick and radiatively-inefficient accretion disk to which we will refer as a *Advection Dominated Accretion Flow* geometry (or just ADAF geometry, Rees et al. 1982; Narayan & Yi 1994). As shown, regardless of the BH mass, $z \sim 3$ active BHs are characterized by a thin disk geometry fuelled by Eddington limited accretion flows (see Fig. 5). This picture changes at $z \sim 0$, where ADAF becomes the main accretion geometry for BHs with $M_{\text{BH}} > 10^6 M_\odot$. In this case, BHs are powered by the quiescent phase of cold gas accretion and the consumption of hot gas which surrounds its host galaxy (see right panel of Fig. 5). We refer the reader to Section 3.2, where a detailed description of how f_{Edd} values are computed in our BH growth model.

Finally, we have also explored the evolution of the black hole masses in the chaotic scenario proposed by King et al. (2005)¹². For the sake of the present discussion, we only compare the main predictions of this *chaotic* model to our findings. We have seen that, as a consequence of the different outcomes in the spin distribution, there is a faster BH assembly in the chaotic model than in the one explored in this work. Whereas the former display typically spin values of $a \lesssim 0.1$, the latter is characterised by $a \gtrsim 0.7$. As shown by Eq.(23), the spin has an impact in the mass-to-energy conversion, implying longer timescales in the BH growth at larger spin parameters (see Eq.(11)). We have also checked that the fast growth undergone by the BHs in the chaotic scenario has an imprint in the faint end of $z \lesssim 1$ bolometric luminosity functions (LFs). Since the BH growth in the chaotic scenario happens on a shorter time-scale than in the model presented here, the BHs tend to consume the gas reservoir faster, hence entering to the quiescent phase earlier. This implies that BHs at low z do not have enough gas in order to effectively contribute to the faint-end of the bolometric luminosity function, reducing its amplitude. In order to contrast this effect and match the observed faint-end of the AGN bolometric LF, the parameters $f_{\text{BH}}^{\text{merger}}$ and $f_{\text{BH}}^{\text{DI}}$ (Eq.(4)-(5)) controlling the amount of gas accreted during mergers and DI, had to be increased. This resulted in a significant excess on the predicted BHMF at $M_{\text{BH}} > 10^8 M_\odot$, making difficult its comparison to observations.

4.2 The evolution of bolometric luminosity

Since the discovery of the first quasar (Schmidt 1963), it has been widely accepted that the quasar phase is triggered by the gas accretion onto BHs. The understanding of the quasar luminosity function at different redshifts is a crucial point for inferring the assembly history of BHs. They provide us with information about the BH growth rate, the nature of accretion disks and fundamental quantities such as BH spins and radiative efficiencies. In the left panel of Fig.5 we present the evolution of the bolometric luminosity (L_{bol}) function predicted by our model (in Appendix B

¹¹ For instance, they reported that local galaxies with black hole mass estimate with a dynamical approach are a biased subset of all galaxies, i.e at fixed stellar mass BHs display larger velocity dispersion than the bulk of the population, regardless of the exact morphological type.

¹² Following Sesana et al. (2014), the chaotic scenario presented in King et al. (2005) is obtained fixing $F = 1/2$ in Eq.(20).

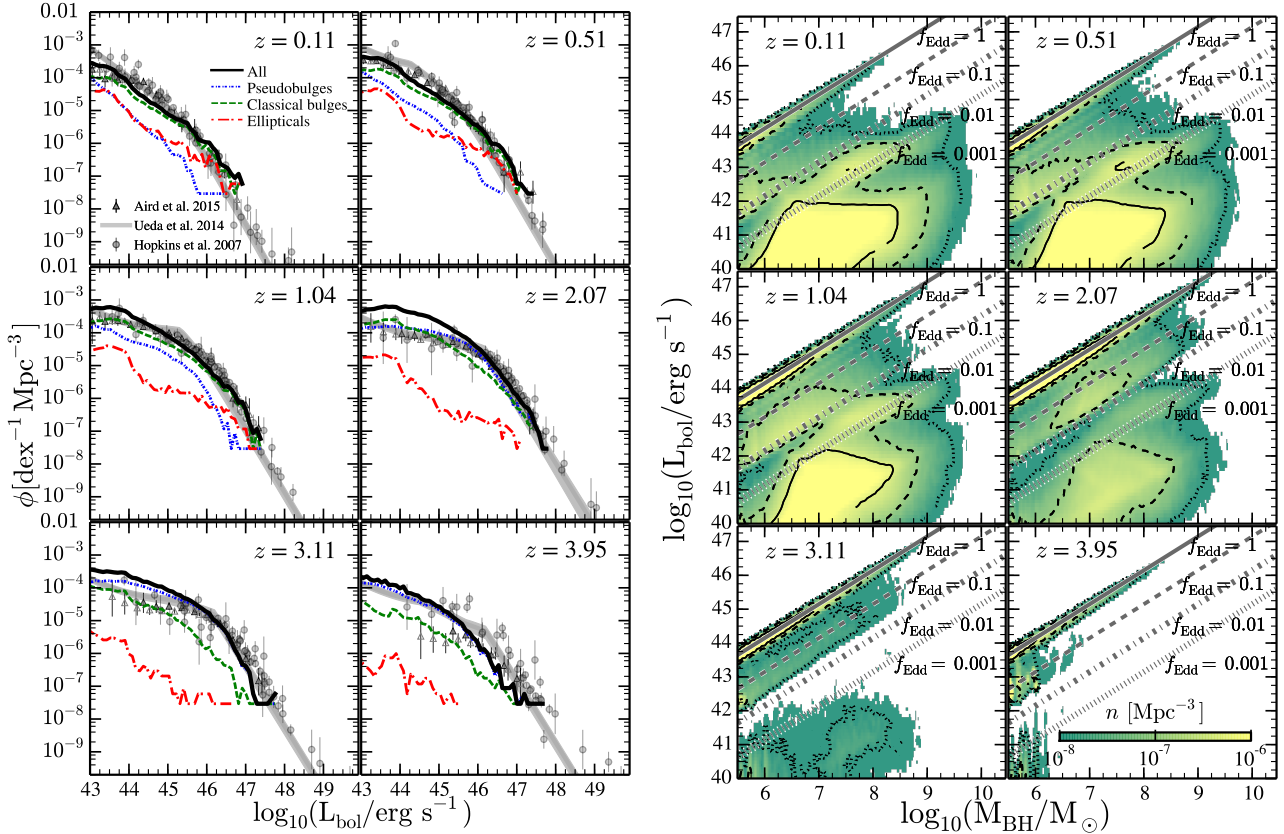


Figure 5. **Left panel:** Quasar bolometric luminosity functions (L_{bol}) at $z \approx 0.1, 0.5, 1.0, 2.0, 3.0, 4.0$. Solid lines represent the total quasar bolometric luminosity functions. Red dashed-dotted line, green dashed line, and blue dotted lines represent the same but for galaxies hosting respectively elliptical, classical bulge, and pseudobulge bulge structures. Luminosity functions are compared with the data of Hopkins et al. (2007) (circles), Aird et al. (2015) (triangles) and the fit of Ueda et al. (2014) (shaded area). **Right panel:** Bolometric luminosity (L_{bol}) - black hole mass (M_{BH}) plane at $z \approx 0.1, 0.5, 1.0, 2.0, 3.0, 4.0$. The color map encodes the number density (n [Mpc⁻³]) of objects, with solid, dashed and dotted contours indicating the regions with n equal to 5×10^{-7} Mpc⁻³, 10^{-7} Mpc⁻³, and 10^{-8} Mpc⁻³, respectively. Diagonal lines represent 1, 0.1, 0.01, and 0.001 f_{Edd} limits.

it is presented the same but for hard and soft X-rays luminosity). The predictions of our model are compared to the observational work of Hopkins et al. (2007); Aird et al. (2015) and Ueda et al. (2014). A good agreement is achieved at any redshift bin. However, at $z < 0.5$ our model slightly underestimates the number of objects in the range of $10^{44} \lesssim L_{\text{bol}} \lesssim 10^{45}$ erg/s. This might be caused by other feeding processes which are not accounted by our model. For instance, Volonteri et al. (2013) discussed that substantial growth of BHs in elliptical galaxies was due to the consumption of recycled gas of the evolving stellar population. In future works, we plan to include this extra growth channel in both elliptical and spiral galaxies. In the same figure, we have divided the luminosity functions in three types of bulge population: galaxies hosting a pseudobulge, classical bulge and elliptical structure. While at high- z ($z > 2$) the bolometric luminosity function is dominated by BHs accreting in pseudobulge structures, at lower redshifts classical bulges and elliptical galaxies are the main structures hosting active BHs. At $z < 1$, pseudobulges host only faint AGNs ($L_{\text{bol}} \lesssim 10^{44}$ erg/s). Since pseudobulges form in galaxies experiencing a quiet merger history (see Izquierdo-Villalba et al. 2019), our model points out that high- z AGNs ($z \gtrsim 2$) and a fraction (~ 10 – 20%) of inter-

mediate luminous AGNs ($L_{\text{bol}} \sim 10^{44-45}$ erg/s) at $z \lesssim 1$ are mainly triggered by secular processes rather than galaxy encounters. This is in agreement with recent observational and theoretical results. For instance, the observational work of Allevato et al. (2011) pointed out that major or minor mergers alone are not able to reproduce the high bias factors of X-ray AGN selected sample. Similar results were obtained in Marian et al. (2019) for X-ray and optical selected AGNs at $z \sim 2$. On the theoretical side, Martin et al. (2018), by using the Horizon-AGN hydrodynamical simulation, found out that only 35% of today's BH mass is directly attributable to merger-driven gas accretion. Similar results were found by Steinborn et al. (2018), which using large-scale cosmological hydrodynamic simulations from the Magneticum Pathfinder set, concluded that mergers could not be the statistically prevalent fuelling mechanism for nuclear activity at $z = 0 - 2$, except for very luminous AGNs, with $L_{\text{bol}} > 10^{46}$ erg/s. From the semi-analytical models perspective, recent works of Lagos et al. (2008); Fanidakis et al. (2011); Griffin et al. (2019) and Marshall et al. (2020) found that, regardless of redshift, DIs are the main drivers of BH growth and AGN activity. Even though all these works use the same analytical prescription to detect instabilities in the galactic disk (see Eq. 1), their

implementation is slightly different from the one used here. For instance, the model of [Fanidakis et al. \(2011\)](#) (and [Griffin et al. 2019](#)) assumes that any disk instability event is able to destroy the galactic disk, transforming the galaxy into a pure spheroidal structure and triggering a burst of star formation. On the other hand, the works of [Lagos et al. \(2008\)](#) and [Marshall et al. \(2020\)](#) follows the approach presented here transferring to the galaxy spheroidal component only the amount of stellar mass needed to restore the disk stability. However, they do not distinguish between their triggering mechanism, as we do here.

To directly explore the relation between bolometric luminosity and BH mass, in the right panel of Fig.5 we show the black hole mass-bolometric luminosity plane at six different redshifts. At $z \gtrsim 3$ there is a tight correlation between black hole mass and luminosity, as almost all BHs are accreting at $f_{\text{Edd}} = 1$. On the contrary, at $z < 2$ most BHs are far from growing at the Eddington limit, and diverse combinations between BH mass and f_{Edd} are present. For instance, whereas at $z \sim 4$ all the quasars shining at $L_{\text{bol}} \sim 10^{45}$ erg/s are triggered by BHs of mass $M_{\text{BH}} \sim 10^7 M_{\odot}$ with $f_{\text{Edd}} = 1$, at $z \lesssim 3$ the same luminosity is triggered by a wide range of BHs ($M_{\text{BH}} \sim 10^7 - 10^9 M_{\odot}$) accreting at $f_{\text{Edd}} \sim 1 - 0.01$. Only the highest luminosity ($L_{\text{bol}} \gtrsim 10^{46}$ erg/s) are reached always by the same type of objects: BHs of mass $M_{\text{BH}} \gtrsim 10^8 M_{\odot}$ accreting at the Eddington limit. Interestingly, the plane $L_{\text{bol}} - M_{\text{BH}}$ displays two branches: one at $f_{\text{Edd}} \gtrsim 10^{-3}$ and the other at $f_{\text{Edd}} \lesssim 10^{-3}$. While the former is caused by cold gas accretion, the latter is originated by hot gas consumption. At $z > 3$ these two regimes are clearly separated, whereas at $z \sim 2$ the branches start to blend. This is because BHs accreting via the cold gas phase enter in the quiescent (or self-regulated) phase, characterized by low f_{Edd} . Eventually, as we discussed in Fig.5 left panel, at $z \sim 0$ the number density of active BHs is dominated by low f_{Edd} values (or ADAF geometries) caused by both hot and cold gas accretion.

4.3 The evolution of black hole spin

Apart from mass, the spin parameter is the other fundamental property of BHs that has to be taken into account to build a complete picture of how black holes assemble their masses across cosmic time, given also the dependence of the radiation efficiency on the spin value. From an observational point of view, spin measurements are still a challenge and the current estimates display large errors. [Reynolds \(2013\)](#) present a compilation of few BHs with reliable measurements of both spin and mass. However, all the spin values have been computed via X-ray spectroscopy of iron $K\alpha$ line, biasing the results towards AGNs with bright hard X-rays luminosity ($\gtrsim 10^{42}$ erg/s, see Table 2 in [Sesana et al. 2014](#)). As a check of the spin predictions in `L-Galaxies`, we present in Fig.6 a comparison of the model with [Reynolds \(2013\)](#) data. In order to perform a fair comparison we have only selected in our sample the BHs with hard X-ray luminosity larger than 10^{42} erg/s (see Appendix B for hard and soft X-rays LFs). We see that the model predictions are overall consistent with the observations.

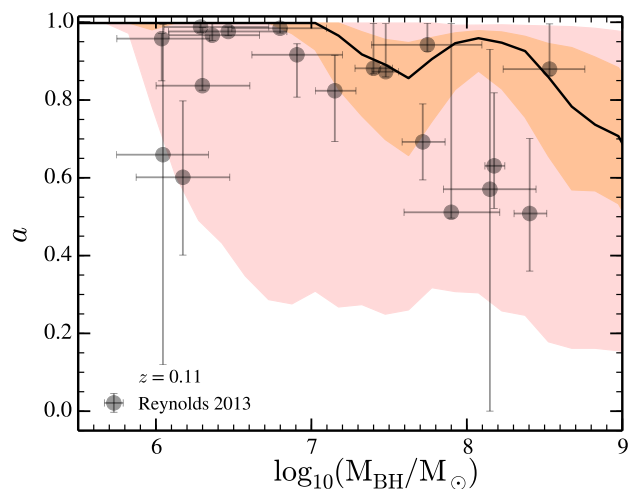


Figure 6. Black hole spin, a , as a function of black hole mass (M_{BH}) at $z=0$ for black holes with hard X-ray luminosity $L_{\text{HX}} > 10^{42}$ erg/s. The solid black line represents the median value of the spin, whereas dark and light orange shaded areas display the 1σ and 2σ of the distribution. Black dots are the observational data of [Reynolds \(2013\)](#).

In the left panel of Fig.7 we present the cosmological evolution of BH spin. The model generally predicts a rapidly spinning super-massive black hole population. While at $M_{\text{BH}} < 10^6 M_{\odot}$ BHs tend to be maximally spinning, at $M_{\text{BH}} > 10^6 M_{\odot}$ BHs display lower spin values (see also [Sesana et al. 2014](#)), with average spin values decreasing with increasing BH mass. Also, the median spin values show a modest decrease with decreasing redshift, but only for BHs with $M_{\text{BH}} > 10^6 M_{\odot}$. The different spins of small and high-mass BHs come from the ratio $|\vec{J}_d|/2|\vec{J}_{\text{BH}}|$ during the gas consumption. At $M_{\text{BH}} < 10^6 M_{\odot}$, independently of the redshift and the nature of the accretion episode, the ratio $|\vec{J}_d|/2|\vec{J}_{\text{BH}}|$ is always larger than one, resulting in a BH feeding characterized by $n_{Pa} = 1$ (see Section 3.3). Conversely, for $M_{\text{BH}} > 10^6 M_{\odot}$, the value of $|\vec{J}_d|/2|\vec{J}_{\text{BH}}|$ is not necessary larger than one and the precise number of n_{Pa} depends on the galaxy bulge assembly. Indeed, this bulge dependence is seen in Fig.7 when the BH population is divided according to the host bulge type (pseudobulge, classical bulge and elliptical). Regardless of the redshift, at fixed mass, BHs hosted in pseudobulges display larger spin values ($a \gtrsim 0.9$) than the ones in classical bulges ($a \sim 0.7$) and ellipticals structures ($a \lesssim 0.4$). This is in agreement with the work of [Orban de Xivry et al. \(2011\)](#), which concluded, by observing local AGN, that BHs in local Narrow-line Seyfert I galaxies (with masses $\sim 10^6 M_{\odot}$) hosted in pseudobulge structures need to be rapidly spinning in order to explain their duty cycles. Notice that the model predicts a slight spin-up of BHs hosted in elliptical galaxies from $z \sim 1$ ($a \sim 0.3$) to $z \sim 0$ ($a \sim 0.4$). This is because after the formation of the elliptical structure the galaxy undergoes successively minor mergers/smooth accretions (a median value of 5) which carry gas with large v/σ towards the BH, ultimately causing its spin-up (see Figure 7 and 16 in [Izquierdo-Villalba et al. 2019](#) where we show the number density of minor/smooth accretion events and the typical

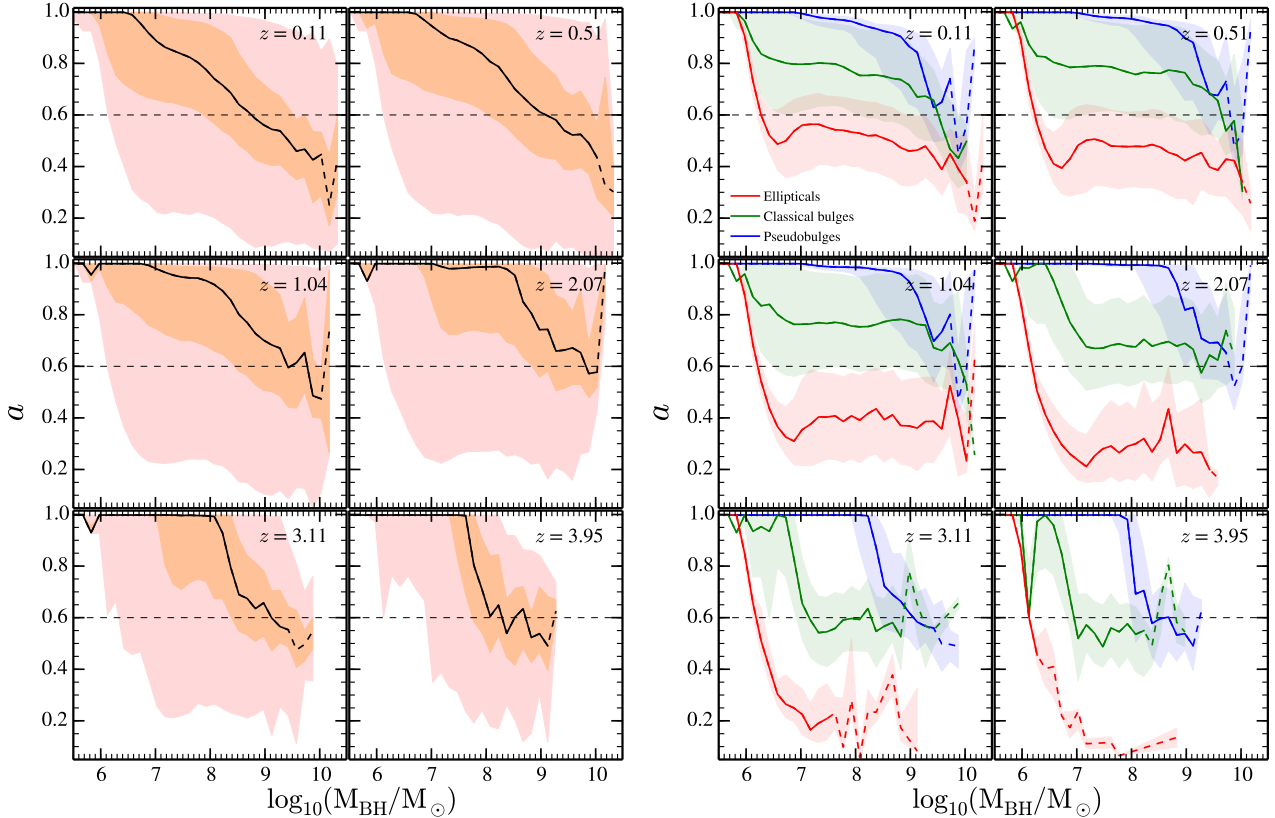


Figure 7. **Left panel:** Predicted black hole spins, a , as a function of black hole mass (M_{BH}) and at different redshifts. Solid black lines represent the median value of the spin per black hole mass. Dark and light orange shaded areas display the 1σ and 2σ of the distribution. To guide the reader we have highlighted with dashed lines the value of $a=0.6$ (corresponding to an accretion efficiency ~ 0.1). **Right panel:** The same as in the left panel but dividing the galaxies between classical bulges (green), pseudobulges (blue) and ellipticals (red). Shaded areas display the 1σ of the distribution. The large fluctuations at high masses are due to small sample statistics (in both panels dashed lines in the median relation corresponds to the black hole masses where the number of objects is smaller than 5).

redshift of the last minor merger). This is along the line of recent observational work, pointing out that minor mergers (~ 8 with mass ratio 1:10) contribute significantly to the build-up of massive elliptical galaxies at $z \lesssim 1$ (Boylan-Kolchin et al. 2006; Trujillo et al. 2011). The dependence on the bulge type is somewhat blurred for BHs with $> 10^8 M_{\odot}$ inhabiting pseudo- and classical- bulge structures. This is because such massive BHs are hosted in massive galaxies ($M_{\text{stellar}} > 10^{11} M_{\odot}$) whose bulge assembly is complicated, shaped by both mergers and disk instabilities. This intricate bulge assembly results in a complex evolution of the bulge v/σ , significantly deviating from the v/σ values produced by DI or minor mergers alone. For instance, the bulge v/σ in pseudobulges decreases after a minor merger while v/σ in classical bulges increases after a DI. Other mechanisms that blur the spin-bulge dependence at $\gtrsim 10^8 M_{\odot}$ are the *gas-poor* BH-BH coalescences. In these cases the remnant BHs do not accrete gas and the spin change is driven by the BH coalescence. Berti & Volonteri (2008) showed that the spin evolution under only BH-BH mergers is driven towards $a \sim 0.4-0.7$ (with some intrinsic dispersion).

During the last years several studies have addressed the evolution of BH spin by using semi-analytical models. For instance, Fanidakis et al. (2011) and Griffin et al. (2019)

found out that the *chaotic* scenario suggested by King et al. (2005) applied on GALFORM SAM (run on top of the Millennium and P-Millennium merger trees) yields a population of BHs characterized by low spin values ($a \lesssim 0.4$) at any mass and redshift (see Figure 9 of Fanidakis et al. 2011 and Griffin et al. 2019). Even though the chaotic scenario was able to reproduce the population of radio-loud AGNs in the local Universe, its outcome spin distribution makes difficult reconciling the model predictions with the recent claims of a rapidly spinning black hole population (Orban de Xivry et al. 2011; Reynolds 2013; Trakhtenbrot 2014; Shankar et al. 2016). In the same work they also explored a *prolonged* accretion scenario. Although in this case the model predicts BHs with $a > 0.9$, the observed LFs are systematically above the observed one and its consistency with radio-loud AGNs in the local Universe is worse than in the chaotic scenario (see Figure 10 of Fanidakis et al. 2011 and Figure 16 of Griffin et al. 2019). Other attempts have been done by Barausse (2012) employing a SAM build on top of Press-Schechter merger trees. By using a more sophisticated approach consisting in feeding the BH respectively in a prograde and chaotic way during gas rich and gas poor mergers, they found a dichotomy in the spin distribution between rapidly ($a \gtrsim 0.9$) and low ($a \sim 0.2$) spinning BHs (see Figure 14 and 15 in Barausse 2012). Sesana et al. (2014) updated the spin

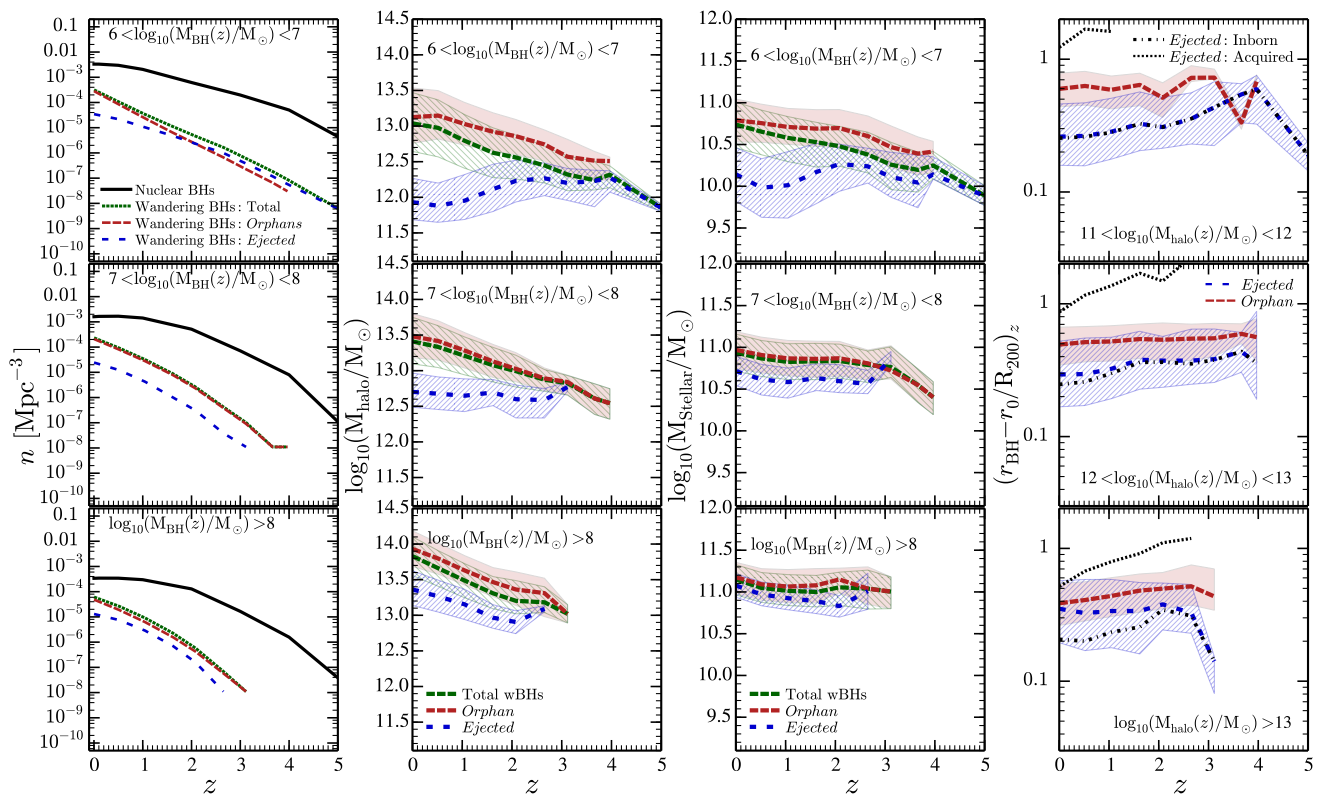


Figure 8. **Left panel:** Redshift evolution of the number density (n) of nuclear (thick black solid line) and wandering (thick short-dashed dark green line) BHs of in the ranges: $6 < \log_{10}(M_{\text{BH}}/M_{\odot}) < 7$ (upper panel), $7 < \log_{10}(M_{\text{BH}}/M_{\odot}) < 8$ (middle panel) and $\log_{10}(M_{\text{BH}}/M_{\odot}) > 8$ (lower panel). The population of wBHs has been divided into *orphans* (long dashed dark red line) and *ejected* (dotted dark blue line). **Central left panel:** Median subhalo mass in which wandering black holes are hosted at different redshifts. As in the left panel, each figure corresponds to a different BH mass bin. The wBH population has been divided into *orphans* (long dashed dark red line) and *ejected* (dotted dark blue line). The shaded areas indicate the 1σ dispersion. **Central right panel:** Same as the central left panel but for stellar masses. **Right panel:** Redshift evolution of the median positions of all wandering black holes with mass $> 10^6 M_{\odot}$. The position, r_{BH} , is given with respect to the subhalo center, r_0 , and is normalized to the subhalo virial radius, R_{200} . Each panel corresponds to a different subhalo mass bin. Blue short-dashed and red long-dashed lines represent the median positions of *ejected* and *orphan* wBHs respectively. The shaded areas indicate the 1σ dispersion. We further split the ejected population into inborn and acquired, represented by the black short-dashed and blue dotted lines, respectively.

evolution of Barausse (2012) by linking the BH growth with the assembly of the galactic bulge. As in this work, they found different spinning black holes hosted in elliptical and spiral galaxies. Finally, Volonteri et al. (2013) also studied the spin with a SAM based on Press-Schechter merger trees. Similar what we do here, they assumed that the BH quasar phase takes place in two different phases. Whereas the former is described by an Eddington limited growth with a spin evolution characterized by a prograde accretion, the latter displays low Eddington ratios with a chaotic spin evolution (even though they explored a coherent mode as well during this quiescent phase). They found a strong spin redshift evolution whereby $z > 2$ BHs are characterized by large spin values ($a > 0.8$) whereas $z < 1$ BHs display small spins ($a < 0.4$). However, the model did not include BH feeding through disk instabilities, a channel which seems to be fundamental in SAMs (Fanidakis et al. 2012; Menci et al. 2014; Marshall et al. 2020).

5 WANDERING BLACK HOLES

In this section we discuss our main results on the wandering black hole population. We first explore the frequency and location of the events at different cosmological times. We then focus on the local universe, investigating the characteristics of wBHs hosted in different kinds of galaxies.

5.1 Wandering black holes across cosmic time

The left panel of Fig.8 shows the redshift evolution of the wBH number density (n). We show only results for BHs whose mass is larger than $10^6 M_{\odot}$ since at smaller masses we can not draw solid conclusions given the resolution of the MS simulation, as previously discussed. Regardless of the BH mass, the number density evolves with redshift, reaching a maximum of $\sim 10^{-3} \text{ Mpc}^{-3}$ at $z \sim 0$. The lighter is the mass of the wBH the larger is the number density at high- z . For instance, while at $z \sim 4$ black holes of $M_{\text{BH}} > 10^7 M_{\odot}$ have $n \lesssim 10^{-6} \text{ Mpc}^{-3}$, black holes of $10^6 < M_{\text{BH}} < 10^7 M_{\odot}$ present 1 dex larger number densities. For comparison, the figure

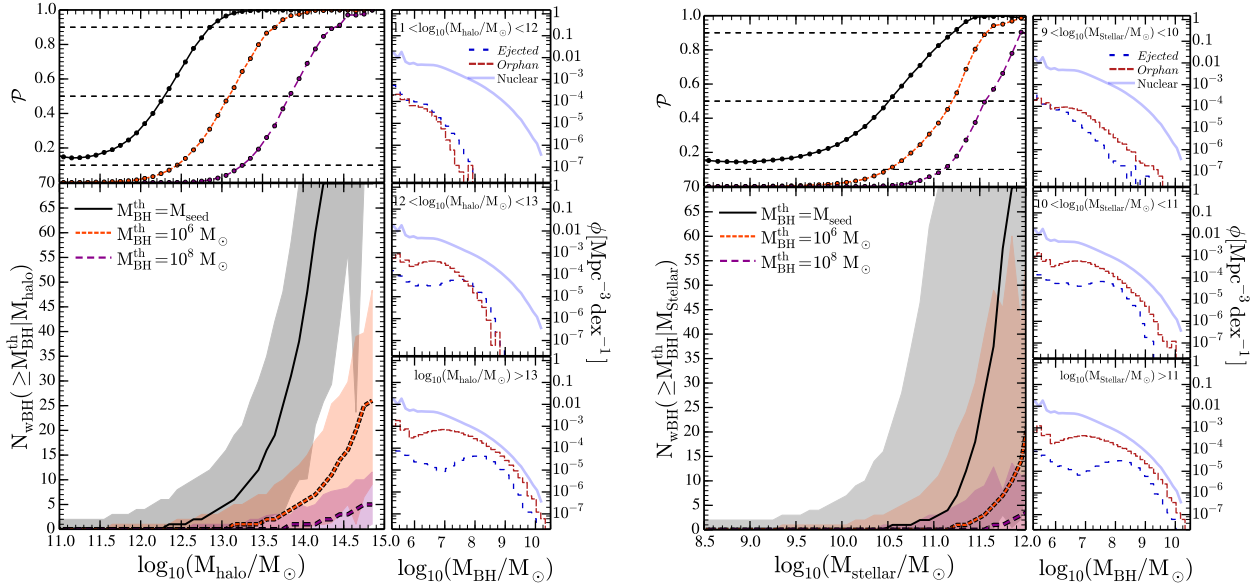


Figure 9. **Left panel:** Connection between the wandering black holes and their host subhalos at $z=0$. *Left upper panel:* Probability \mathcal{P} at a given subhalo mass bin of finding at least one wBH above the mass threshold, $M_{\text{BH}}^{\text{th}}$. Solid black line, short dashed orange line and long dashed purple line display three different $M_{\text{BH}}^{\text{th}}$ thresholds: $M_{\text{seed}} = 10^4 M_{\odot}$, $10^6 M_{\odot}$ and $10^8 M_{\odot}$, respectively. Horizontal dashed lines highlight the values $\mathcal{P} = 0.1, 0.5, 0.9$ the *Left lower panel:* Median number of wandering black holes, N_{wBH} , per subhalo mass bin for a given $M_{\text{BH}}^{\text{th}}$ value. Shaded areas represents the 3σ interval of the distributions. *Right panels:* Wandering black hole mass function at three different subhalo mass bins. Solid blue, short red dashed and long blue dashed lines represent, respectively, the mass function for nuclear BHs, *orphan* wBHs and *ejected* wBHs. **Right panel:** Same as in the left panel but for stellar masses.

displays the n values of nuclear black holes. Regardless of mass and redshift, nuclear BHs are 1–3 dex more numerous than wandering BHs, especially at $z \gtrsim 4$. Concerning the different contribution between *orphan* and *ejected* BHs, we find that at $M_{\text{BH}} > 10^7 M_{\odot}$ the former dominate the number density of wBHs. On the other hand, at $10^6 < M_{\text{BH}} < 10^7 M_{\odot}$ the relative contribution of the two types of wBHs evolves with redshift; while *ejected* wBHs display larger number density at $z \gtrsim 1.5$, *orphan* ones dominate at lower redshifts. This evolution is due to the fact that towards lower z the number of orphan galaxies increase, and, at the same time, the frequency of the *major/minor* interactions decreases (see, e.g., Figure 3.2 of Izquierdo-Villalba et al. 2019).

In the two central panels of Fig.8 the evolution of the median subhalo and stellar mass in which wandering black holes are hosted is presented. At $z > 3$ wBHs with $M_{\text{BH}} > 10^8 M_{\odot}$ inhabit very massive subhalos and galaxies, with typical masses of $M_{\text{halo}} > 10^{13} M_{\odot}$ and $M_{\text{stellar}} > 10^{11} M_{\odot}$. Particularly, the host subhalo mass presents an increasing trend toward low z , displaying values from $M_{\text{halo}} \sim 10^{13} M_{\odot}$ at $z \sim 4$ up to $M_{\text{halo}} \sim 10^{14} M_{\odot}$ at $z \sim 0$. On the contrary, the stellar mass of their central galaxy hardly changes, maintaining a rather constant value of $\sim 10^{11} M_{\odot}$. WBHs with $10^7 < M_{\text{BH}} < 10^8 M_{\odot}$ display a similar behavior but are hosted in slightly less massive subhalos and galaxies. Finally, wBHs with $10^6 < M_{\text{BH}} < 10^7 M_{\odot}$ are typically placed in $M_{\text{halo}} \sim 10^{12.2} M_{\odot}$ and $M_{\text{stellar}} \sim 10^{10.5} M_{\odot}$. When the population of these wBHs is divided by formation scenario, we see that at $z < 2$ *ejected* wBHs tend to be hosted in less massive subhalo and galaxies ($M_{\text{halo}} \sim 10^{11.7} M_{\odot}$ and $M_{\text{stellar}} \sim 10^{10} M_{\odot}$, respectively) than at higher redshifts.

However, the significance of this trend change is small.

The position of both *ejected* and *orphans* wBHs with $M_{\text{BH}} > 10^6 M_{\odot}$ as function of redshift is presented in the right panel of Fig.8. The population has been divided in 3 different bins of subhalo masses while the distances (referred to the halo center, r_0) have been normalized by the subhalo virial radius, R_{200} . As shown, regardless of subhalo mass, *ejected* and *orphan* wBHs at $z > 0.8$ are located in different regions inside the subhalo. While the former reside at $\lesssim 0.3R_{200}$ (with a decreasing trend towards low z), the latter orbit at $\sim 0.6 - 0.8R_{200}$ radii. On the contrary, at $z < 0.8$ there are differences from a subhalo mass bin to another. While for $M_{\text{halo}} < 10^{13} M_{\odot}$ *ejected* and *orphans* wBHs still inhabit different subhalo regions, at $M_{\text{halo}} > 10^{13} M_{\odot}$ both types of wBHs are at similar distances from the subhalo center, $\sim 0.3R_{200}$. To understand this behavior, in Fig.8 we divided the population of *ejected* wBH in two sub-classes: the acquired and inborn ones. While the former have been incorporated from other galaxies after an subhalo merger, the latter were generated in-situ, expelled from the central galaxy of the subhalo after a recoil. A completely different behavior is seen for the two populations, regardless of the redshift. While inborn *ejected* BHs are closer to the subhalo center than orphan BHs, the acquired *ejected* wBHs populate similar regions, further from the subhalo center. Consequently, the change of trend of the *ejected* population in massive subhalos at low z it is caused by the acquired *ejected* wBHs, whose number becomes dominant with respect to the inborn ones.

5.2 The environment of wandering black holes in the local universe

We now focus on the local universe, exploring the typical halo and galaxy masses hosting wandering black holes as well as the frequency of wandering BHs for different galaxy type. As discussed before, we assume that wBHs are not accreting, thus not observable as active sources. In future works we will explore how simple assumptions for the growth of wBHs could translate into their observability for different host properties.

The mass function of wBHs at different subhalo and galaxy masses is presented in the the small panels of Fig.9. For what concerns the subhalo mass, we note that only the more massive subhalos host a significant population of wBHs, including some with mass larger than $10^7 M_\odot$. By dividing the wandering BHs by formation scenario we can see that for $M_{\text{halo}} \lesssim 10^{13} M_\odot$ the *ejected* population reaches larger masses than the orphan one, whereas at larger subhalo masses the trend is inverted. Indeed, the amplitude of the *orphan* wBHs mass function increases with subhalo mass due to the increase of the average number of satellite galaxies¹³. Analogously, galaxies with the largest masses are the ones which host the most massive wandering black holes, but already galaxies with $M_{\text{stellar}} \sim 10^{10} M_\odot$ can be surrounded by massive wBHs.

The larger panels of Fig.9 present both the probability \mathcal{P} of finding at least one wBH above a given mass threshold $M_{\text{BH}}^{\text{th}}$ (upper panel) and the median number of wBHs (N_{wBHs}) at a given subhalo mass (lower panel). Independently of the $M_{\text{BH}}^{\text{th}}$, both \mathcal{P} and N_{wBHs} increase with the host subhalo and galaxy mass. However, the exact value of $M_{\text{BH}}^{\text{th}}$ has an important effect in the values of \mathcal{P} and N_{wBHs} . For instance, at $M_{\text{BH}}^{\text{th}} = M_{\text{seed}}$ all subhalos above $10^{13} M_\odot$ (galaxies above $10^{10.75} M_\odot$) host at least one wBH, with a typical $N_{\text{wBHs}} > 5$. However, only subhalos above $10^{14} M_\odot$ (galaxies above $10^{11.5} M_\odot$) host a wBH with $M_{\text{BH}}^{\text{th}} > 10^8 M_\odot$.

6 THE IMPRINT OF GRAVITATIONAL RECOIL ON THE BH GLOBAL PROPERTIES

In this section we investigate the effects of gravitational recoil in the properties of nuclear black holes across cosmic time. As we will show, long wandering phases can have a visible effect in the black hole occupation fraction and in the BH growth, in particular for certain galaxy types.

6.1 Black hole occupation fraction

The seeding procedure followed in this works (see Section 3.1) imply that all galaxies host a BH when they are initialized. But gravitational recoil after BH mergers can

¹³ Typically, the average number of satellite galaxies increases with the subhalo mass in a power-law shape (see e.g. Berlind et al. 2003; Contreras et al. 2017).

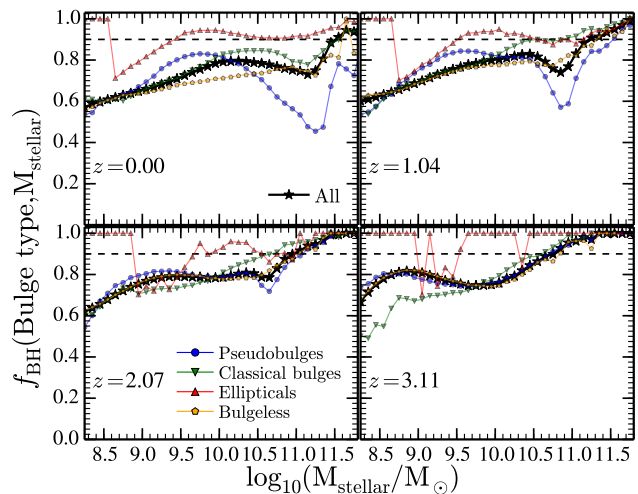


Figure 10. Nuclear black hole occupation fraction, f_{BH} , as a function of stellar mass and different bulge morphological types at $z \sim 0, 1, 2, 3$. Black lines present the f_{BH} for all the galaxies. Blue, green, red and, yellow lines display the break-up into pseudobulges, classical bulges, ellipticals and bulgeless galaxies, respectively. Horizontal dashed line highlights $f_{\text{BH}} = 0.9$.

leave galaxies without a central BH, at least until the kicked BH loses the acquired energy and settles again in the galaxy center. Therefore, especially at later times, a fraction of galaxies is expected to be deprived of a central BH. In Figure 10 we show the nuclear BH occupation fraction as a function of galaxy stellar mass, and for different galaxy morphologies. Regardless of the bulge morphology and redshift, f_{BH} decreases towards *low stellar masses*: from $\sim 80\%$ for $M_{\text{stellar}} \gtrsim 10^{11} M_\odot$ down to $\sim 60\%$ for galaxies with $M_{\text{stellar}} \lesssim 10^{8.5} M_\odot$. This mass dependence is related to the potential well of the galaxy: the smaller the galaxy, the lower the escape velocity, thus the higher the ejection probability for the central BH. Moreover, as we will see at the end of this section, for galaxies with $M_{\text{stellar}} < 10^9 M_\odot$, it is also much more probable the ejection not only from the galaxy, but also from the subhalo. By dividing the galaxy population in different bulge morphological types, we find that, in massive galaxies with $M_{\text{stellar}} > 10^{10} M_\odot$, pseudobulges and bulgeless galaxies display lower occupation fractions than both classical bulges and ellipticals. This is because pseudobulges and bulgeless galaxies experience very few mergers during their evolution, thus it is more difficult for them to replenish their empty bulge after an ejection. Indeed, as we will see in Section 6.2 (Fig.13), the reincorporation of BHs in a pseudobulge galaxy is not very common ($\lesssim 10\%$ of probability at any stellar mass) making it even more difficult for such structures to increase their nuclear BHs occupation fraction. Besides mass and morphology, Fig.10 shows a trend of decreasing f_{BH} towards low z . This is because BH-BH mergers are characterized by smaller values of q ($\sim 0.01, 0.08, 0.1$ for pseudobulges, classical bulges and ellipticals, respectively) and poorer gas environments towards low z . For instance, at $z \sim 2$, 80% of BH-BH mergers in pseudobulges, classical bulges and elliptical galaxies are considered as wet mergers. On contrary, at $z \sim 1.0$, $\sim 90\%$, 60% , 80% of the BH-BH mergers

in pseudobulges, classical bulges and elliptical galaxies are classified as gas poor mergers. These conditions increase the modulus of the kick velocity making it easier for a BH to be ejected. In particular, the recoil velocity after a BH-BH coalescence in a gas-rich environment is generally larger than in a gas-poor one since this latter is inefficient in leading the alignment between the two BH spins. On the other hand, small values of q lead to larger kicks since the recoil value is proportional to the inverse of $(1+q)$ (see Eq. (31)).

To explore in which moment the BH recoil velocities had major importance in driving ejections, Fig.11 shows the comoving number density of BH ejections. Clearly, at $z \sim 1.5$ the number density reaches a maximum, coinciding with the peak of the galaxy-galaxy merger frequency (see Figure 2 in Izquierdo-Villalba et al. 2019). By dividing the ejections in different bins of BH mass we find that the larger is the BH mass, the lower is the redshift of its ejection. While black holes of $< 10^6 M_\odot$ are typical ejected at $z \gtrsim 2.5$, the ones with $> 10^8 M_\odot$ were *kicked out* at $0.1 < z < 0.6$. This mass segregation is just a growth matter. At very high- z we do not find massive BHs ($> 10^8 M_\odot$) being ejected, since they did not have enough time to accrete gas and grow.

Finally, in Fig.11 we also show the number density of reincorporation as compared to the one of ejections. The latter is larger than former by a factor of 2–3 depending on the exact redshift. This is because gravitational recoil would expel more easily a BH from both galaxy and subhalo, rather than only from the galaxy. In other words, gravitational kicks are likely to overcome at once both the subhalo and galaxy escape velocities rather than only the galaxy one. This directly reduces the effective number of BHs that can be reincorporated in the parent galaxy. For instance, regardless of redshift, we have found that galaxies with $M_{\text{stellar}} < 10^9 M_\odot$, $10^9 < M_{\text{stellar}} < 10^{10} M_\odot$, $10^{10} < M_{\text{stellar}} < 10^{11} M_\odot$ have, respectively, 2.5, 2 and, 1.5 times *more* galaxy+subhalo ejections than only galaxy ejections. On the other hand, in more massive systems ($M_{\text{stellar}} > 10^{11} M_\odot$) the trend is inverted and the former is 2 times less common than the latter. A similar behavior is seen with subhalo mass.

6.2 Effects on the scaling relations

As we have seen in the previous section, the population of nuclear black holes is affected by the physics of gravitational recoil included in the model. In this section we explore how this translates into predictions for the bulge-black hole $z=0$ relation.

The left panel of Fig.12 shows the bulge-black hole scaling relation for *all* galaxies when the SAM is run including or not both BH recoil velocities and wandering phase. Clearly, the scatter and the median relation are different in the two runs. The model displays a trend of hosting less massive BHs at fixed bulge mass in the run in which recoil velocities and wandering phase are taken into account. In the other two panels the population is divided by bulge morphological type: classical bulges and ellipticals (middle

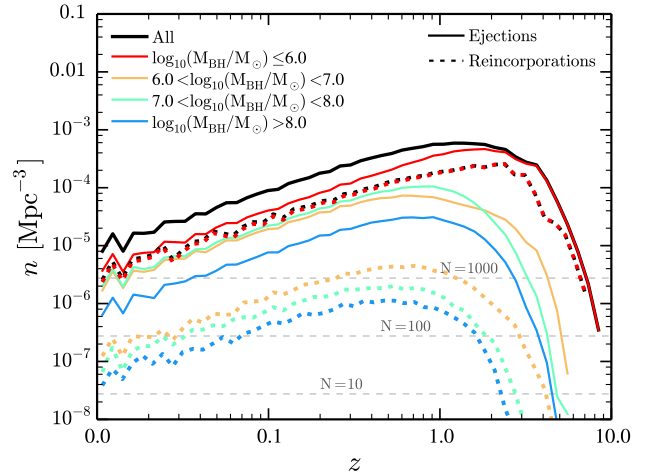


Figure 11. Redshift distribution of black hole ejections via gravitational recoils (solid lines) and reincorporation after a wandering phase (dashed lines). While black lines represent the predictions for the whole BH population, different colors are for different black hole mass bins as labeled in figure. Horizontal grey lines display the values of n in which we have a number of objects ($N = n(z) \times L_{\text{Box}}^3$) equal to 10, 100 and 1000.

panel) and pseudobulges (right panel). While we still see some effects in the classical bulge population, the signatures of BH recoil are more pronounced for the pseudobulge population, where the median relation at $M_{\text{bulge}} \gtrsim 10^{10} M_\odot$ changes up to ~ 2 dex and the scatter increases up to 4 dex.

These results clearly show that the inclusion of gravitational recoil physics is important in the predictions for the BH scaling relations, in particular in pseudobulge galaxies. Similar effects were found in the hydro-simulations of Blecha et al. (2011) and the analytical model of Gerosa & Sesana (2015). By running over 200 simulations of gaseous galaxy mergers with 60 different BH-BH merger configurations Blecha et al. (2011) found out that the inclusion of gravitational recoils leaves an imprint in the correlation between bulge velocity dispersion and the mass of the host BH. At fixed BH mass, the run with gravitational recoils displays large bulge velocity dispersion values. This deviation is caused by the ejection interrupting the BH growth while the galaxy continues its evolution. On the other hand, the work of Gerosa & Sesana (2015) explored the repercussion of gravitational recoils in brightest cluster galaxies (BCGs). They pointed out that the ejections and subsequent replenishments of BHs after galaxy mergers increase the scatter of the BCGs black hole - bulge mass relation.

In Fig.13 we explore in more details the origin of the deviations of the recoiled population with respect to the median relation. We again present results for classical bulges (left panel) and pseudobulges separately (right panel). The median relation is divided into galaxies whose nuclear BHs never underwent an ejection nor a wandering phase (G_0), galaxies whose bulge did not host a central BHs but

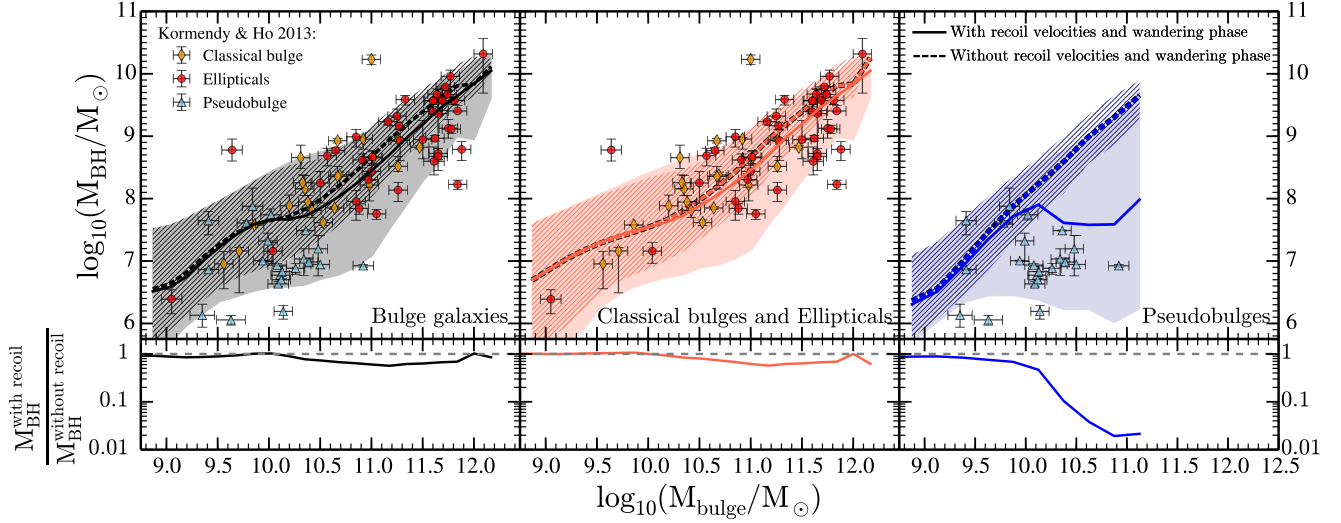


Figure 12. Upper panels: Black hole mass (M_{BH}) - bulge mass (M_{Bulge}) scaling relation in the local universe ($z=0$). Left panel represents the relation for the entire galaxy population, the central panel is for classical bulges and elliptical galaxies, and the right panel is for pseudobulges. Solid and dashed lines represent, respectively, the median of the relation when the SAM is run with and without including recoil velocities and wandering phase. Plain and dashed shaded area represent, respectively, the 2σ of the relation with and without recoil velocities. Dots display the data from Kormendy & Ho (2013). **Lower panels:** Ratio, at a fixed bulge mass, between the black hole mass in the model with recoil velocities and the black hole mass in the model without recoil velocities.

after a merger¹⁴ it was refilled by one (G_{refill}) and galaxies whose BHs were reincorporated after a wandering phase (G_{reincop}). Regarding pseudobulges, galaxies belonging to G_0 follow a very similar relation as the model without recoil velocities (see Fig.12). A similar trend is visible for the galaxies type G_{refill} at $M_{\text{bulge}} \lesssim 10^{10} M_{\odot}$. However, their trend breaks at larger bulge masses. Concerning galaxies of type G_{reincop} , they show a much more flattened relation compared to the previous ones, regardless of bulge mass. This is because the merger (principally *smooth accretions*) that filled the pseudobulge happened at relatively low z , typically $z \lesssim 1.0$, with a galaxy hosting a BH that is ~ 2 dex ($q \sim 0.01$) lighter than the average BH that would inhabit the empty bulge. As shown in the upper panel of Fig.13, the relative contribution of G_0 , G_{refill} and, G_{reincop} causes the change on the pseudobulge scaling relation with respect to the one without recoil velocities. Since galaxies G_0 are the dominant ones at $M_{\text{bulge}} < 10^{10} M_{\odot}$ we do not find any differences between the model with and without BH recoils. However, at $M_{\text{bulge}} > 10^{10.2} M_{\odot}$ the trend changes since galaxies type G_{reincop} take the main importance, causing the flattening in the relation, seen in Fig.12.

Concerning classical bulges and ellipticals structures, all the three types G_0 , G_{refill} and, G_{reincop} have similar bulge-BH mass relation than the relation without recoil (even though G_{reincop} is systematically below). This is caused by the fact that classical bulges and elliptical galaxies do not spend a lot of time without a BH: the reincorporation time of the BH is relatively low ($\lesssim 0.01$ Gy) and since their formation is linked with the hierarchical growth of structures, they experience frequent mergers

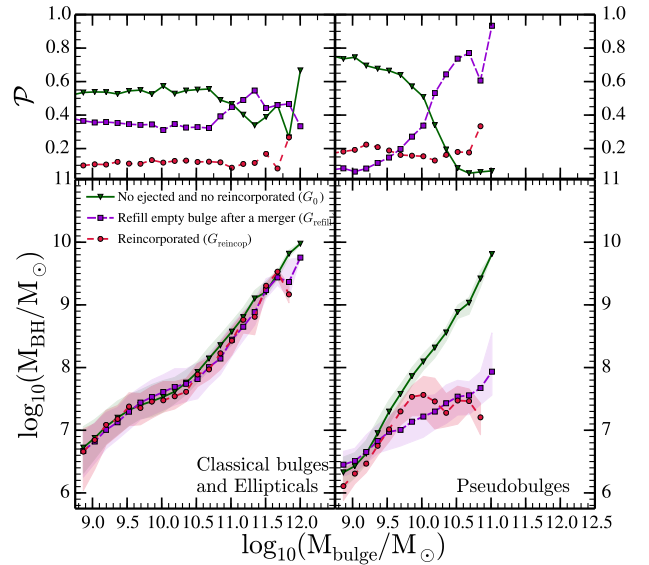


Figure 13. Upper panels: Probability, for a given bulge mass, of finding a nuclear BH which never underwent an ejection nor a wandering phase (G_0 , green line), a nuclear BH which refilled an empty bulge after a merger (major, minor or *smooth accretion*, G_{refill} , violet line) and a BH which was reincorporated after a wandering phase (G_{reincop} , red line). **Lower panels:** Scaling relation for classical bulges plus ellipticals (left panel) and pseudobulges (right panel) when the nuclear BH inhabiting that bulge morphology is divided in the three previous types.

(with $q \gtrsim 0.2-0.3$) in short time-scales. As it is shown in the upper panel of Fig.13, galaxies G_0 dominate at any bulge masses. However, at $M_{\text{bulge}} > 10^{10.5} M_{\odot}$ the probability \mathcal{P} of

¹⁴ major, minor or *smooth accretion*.

finding a galaxy G_{refill} increases up to $\mathcal{P} \sim 0.4$. This causes the small change seen in the relation with and without recoil velocities in Fig.12. We have also explored the G_0 , G_{refill} and, G_{reincop} population at $z=2$ for both classical bulges (and ellipticals) and pseudobulges. In this case, at any mass and bulge type the G_0 population dominates. For instance, at $M_{\text{bulge}} \sim 10^{10.5} M_{\odot}$ G_0 counts for more than the 65% and 80% of the population of classical bulges and pseudobulges, respectively. This causes the median value in the runs with and without recoil velocities to be very similar, even though the population G_{refill} and G_{reincop} helps in increasing the scatter.

In a test run, we have also checked how the bulge-black hole scaling relation behaves when in the model we do not assume any correlation between BH accretion and bulge assembly (see Eq.(20)). For that we have run L-Galaxies with the *chaotic* scenario of King et al. (2005) which assumes an isotropic distribution for the angular momentum of the gas clouds¹⁵. We did not find significant differences, as the strength of the recoil velocities depends primarily on the capability of the gas surrounding the BBH in aligning the two BH spins at the moment of the merger, rather than on the spin value. BH-BH coalescences at $z \lesssim 1.5$ are mostly happening in gas poor environments, reducing the number of BH mergers with a spin alignment, independently on the spin model used.

Finally, even though we have showed that reincorporated BHs have small impact in the bulge - black hole mass relation, in Fig.14 we have explored the effect of the BH reincorporation after a wandering phase in the scaling relations. In the figure it is shown the scaling relation for only classical bulges (including ellipticals) and pseudobulges whose central black hole was reincorporated after undergoing a wandering phase. Independently of the bulge morphology, there is a segregation by time in the wandering phase (t^{wand}): BHs which underwent longer wandering phase are systematically below the scaling relation, as growth in the model is only allowed when BHs are centrals (see Section 3.5). This trend is more clear in the pseudobulge population.

7 SUMMARY AND CONCLUSIONS

In this paper we have studied the mass assembly, spin evolution and environment of both nuclear and wandering supermassive black holes. To do that, we have updated with new physical prescriptions the Izquierdo-Villalba et al. (2019) version of L-Galaxies semi-analytical model (SAM). The new prescriptions have been applied to the merger trees of the Millennium simulation, although galaxies have been initialized using the outputs of the higher-resolution simulation MillenniumII.

The starting point of our BH model is the gas accretion from a *hot* and *cold* phase. While the former is linked with the consumption of part of the hot gas atmosphere which

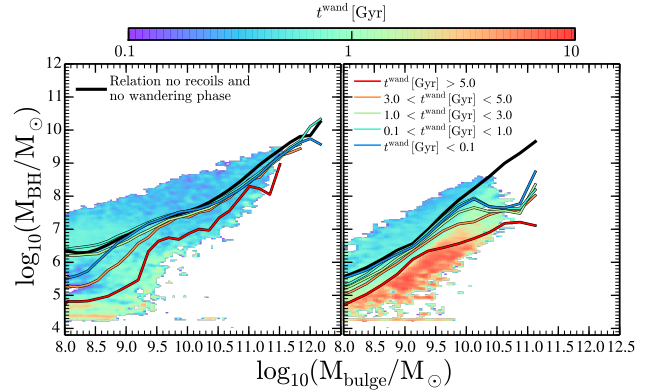


Figure 14. Bulge - black hole mass relation for classical bulges plus ellipticals (left panel) and pseudobulges (right panel) when *only* nuclear black holes which underwent a wandering phase are selected. The color map indicates the median value of the time spent in the wandering phase (t^{wand}) per bin of bulge and black hole mass. In each panel, the solid black line represents the scaling relation when no recoil velocities and wandering phase are included, whereas colored lines represent the median relation for nuclear BHs in a given bin of wandering phase, as labeled in figure.

surrounds the galaxy, the latter is triggered by cold gas accretion right after a galaxy disk instability (DI) and/or a galaxy merger. During both phases of gas accretion, we track the evolution of BH spin (a) using the approach presented in Dotti et al. (2013) and Sesana et al. (2014). We linked the number of prograde transient accretion disk (BH spin-up) with the degree of coherent motion in the bulge. In particular, we have assumed that DIs, which lead to the bar/pseudobulge formation in our model, are the processes that increase the coherence of the bulge kinematics. On the other hand, mergers, which lead to the assembly of classical bulges and ellipticals, bring disorder to the bulge dynamics. These assumptions result in a correlation between the predicted BH spin values and the host galaxy morphology. Regardless of redshift and BH or bulge mass, galaxies with a pseudobulge structure host nuclear BHs with larger spin values than both classical and elliptical galaxies. In particular, at $M_{\text{BH}} > 10^6 M_{\odot}$ pseudobulges, classical bulges and elliptical galaxies host respectively BHs with a typical spin of $a \sim 0.9$, 0.7 and 0.4. At lower BH masses, as a consequence the implemented model, all the three bulge morphology host maximum spinning BHs. The model also follows the formation of binary black hole (BBH) systems by assuming that the lifetime of a BBH (from the formation to the coalescence) inversely correlates with the BH merger ratio and the galaxy gas fraction at the moment of the galaxy encounter. This simple assumption will be further improved in future works. After coalescence, the remnant has a spin value fully determined by the Barausse & Rezzolla (2009) analytic expression.

Due to conservation of linear momentum, in the instant of the BH-BH coalescence the propagation of gravitational waves imparts a recoil velocity to the remnant black hole. If the modulus of the recoil velocity, computed according to Lousto et al. (2012) equations, is larger than the escape

¹⁵ Following Sesana et al. (2014), the chaotic scenario presented in King et al. (2005) is obtained fixing $F = 1/2$ in Eq.(20).

velocity of the host galaxy, the model assumes that the black hole is kicked from its host and incorporated in the DM subhalo as a *wandering black hole*. Here we tag these BHs as *ejected* wBH. Since it is not clear which is the amount of mass in accretion disk that can be retained or accreted by a BH after the recoil, we have neglected the fact that the ejected BH can retain an accretion disk. The model also tracks the formation of another type of wandering black holes, *orphan* wBH, which are originated after the complete disruption of their host galaxy via tidal forces. Independently of their origin, wBH orbits are tracked by using numerical integration, taking into account the host subhalo and galaxy properties for the computation of gravitational acceleration and dynamical friction. In particular, the integration of the wBH orbit stops when i) the black hole is re-incorporated in the galaxy, i.e., when the BH passes through the galaxy center with a velocity smaller than its escape velocity, ii) the recoil velocity of ejected BHs is larger than the subhalo escape velocity or iii) the black hole position exceed 3 times the hosts subhalo virial radius and it is still moving away from the galaxy.

Turning to the model predictions, we find a good consistency with the observed local black hole mass function (BHMF), spin values, BH-bulge mass relation and quasar (bolometric, soft and hard X-rays) luminosity functions. The model predicts a stalling in the BHMF at $z \sim 1$, where no significant change up to $z=0$ is shown. This indicates that most of the local BHs were already assembled by $z \sim 1$. By dividing the BHs between inactive and active we have found that the former population increases from $z \sim 3$ to $z \sim 0$, with the most massive BHs becoming non-active earlier. The accretion geometry of the active population displays also a redshift evolution. Regardless of BH mass, $z \sim 3$ active BHs are characterized by a thin disk geometry fuelled by Eddington-limited accretion flows. ADAF, instead, becomes the main accretion geometry at $z \sim 0$ for BHs with $M_{\text{BH}} > 10^6 M_{\odot}$, powering BHs during the quiescent phase of cold and hot gas accretion. On top of this, the luminosity functions of the model indicate that accreting BHs are hosted in different bulge morphologies at different cosmological times. While at $z > 2$ the high end of the luminosity function is dominated by BHs accreting in pseudobulge structures, at lower redshifts classical bulges and elliptical galaxies are the main structures hosting the most powerful active BHs. Since in the SAM the pseudobulge formation is detached from the merger framework (see Izquierdo-Villalba et al. 2019) our model points out that $z \gtrsim 2$ AGNs are mainly triggered by secular processes instead of galaxy encounters, in agreement with recent observational and theoretical results.

One of the main novelties of the present study is a thorough exploration of the population of wandering black holes (wBHs), either *orphan* or *ejected*. When looking at their mass density, we have found an increasing trend towards low z , reaching a maximum of 10^{-4}Mpc^{-3} at $z \sim 0$, which is considerable but still 1–3 dex smaller (depending the BH mass) than that of nuclear black holes. Regarding the spatial distribution, *ejected* and *orphan* wBHs occupy different regions inside the subhalo. While the former reside at $\lesssim 0.1 R_{200}$, with a decreasing trend towards low z , the

latter inhabit the $\gtrsim 0.2 - 0.4 R_{200}$ regions. Concerning the environments of wBHs in the local universe, the model predicts that subhalos of $M_{\text{halo}} < 10^{13} M_{\odot}$ rarely host a wBH with $> 10^6 M_{\odot}$. But if they do, the wBH is typically formed after a gravitational recoil, i.e. of the *ejected* type. The picture is inverted at $M_{\text{halo}} > 10^{13} M_{\odot}$, where it is relatively more common to find a wBH of $M_{\text{BH}} > 10^6 M_{\odot}$ (typical ~ 5) principally formed after the disruption of satellite galaxies, i.e. of the *orphan* type. We find the same tendency when looking at wBH statistics against the host stellar mass.

Besides being an important channel of wandering black hole formation, we have found that gravitational recoils also affect the co-evolution between the black hole and the host galaxy. In particular, they cause a systematic depletion of nuclear BHs towards low redshift and stellar mass. While the former dependence is because low- z BH-BH coalescences are characterized by poorer gas environments than the ones at higher- z , condition which increase the modulus of the kick velocity, the latter is simply caused by the fact that low-mass galaxies have smaller potential wells than massive ones, making it more difficult for them to retain the BH after a kick. By dividing the galaxy population according to bulge type, we have found that at $M_{\text{stellar}} \gtrsim 10^{10} M_{\odot}$ both classical bulge and elliptical structures tend to display larger occupancy fractions than pseudobulges and bulgeless galaxies. This behavior is due to the fact that pseudobulges are detached from the merger framework, making more difficult for them to replenish their empty bulge after an ejection. On the other hand, at $M_{\text{stellar}} \lesssim 10^{10} M_{\odot}$ classical bulges are more affected by the gravitational recoils, having more than the 40% of empty bulges. By running the SAM with and without gravitational recoils and wandering phase we have also explored the imprints of gravitational recoils in the $z=0$ bulge-BH scaling relation. We have found that both the median of the relation and its scatter are different in the two runs. There is a trend of hosting less massive BHs at fixed bulge mass in the run in which recoil velocities and wandering phase are taken into account. A similar tendency is found when the population is divided into classical bulges, elliptical galaxies and pseudobulges. In particular, the latter structures are the ones which suffer a more pronounced effect, where the median relation at $M_{\text{bulge}} \gtrsim 10^{10} M_{\odot}$ changes ~ 2 dex and the scatter increases. Finally, we have also explored the effect of BH reincorporation after a wandering phase in the BH-bulge relation. Regardless of bulge morphology, the larger is the time of the BH in the wandering phase before its reincorporation, the larger is its offset from the median BH-bulge relation.

Despite the model presented here represents a considerable step forward in modeling the evolution of the population of black holes across cosmic time, still more effort is needed to construct a full coherent framework that can produce new quantitative predictions that can be tested against current and future observations. For example, including a physical model for the expected activity of wBH will lead to useful predictions about the number of active wBHs that may be observed in the local Universe and their more likely location with respect to their host galaxy/group/cluster. In the near future, new instrumentation will make it possible to constrain several aspects of the cosmic BH formation and

evolution. The *Laser Interferometer Space Antenna* (LISA, [eLISA Consortium et al. 2013](#)) will constrain the nuclear BH merger rate and their spin properties, thus also providing precious information for the theoretical modeling of the *kicked* wBH population; *James Webb Space Telescope* (JWST, [Gardner et al. 2006](#)) and *Advanced Telescope for High-ENergy Astrophysics* (ATHENA, [Nandra et al. 2013](#)) will allow to pierce deeper in the cosmos, probing progressively further and lower mass accreting BHs. Only a concerted interplay of theory and observations will unfold the full history of the cosmic, nuclear and wandering, supermassive black hole population.

ACKNOWLEDGEMENTS

We thank the anonymous referee for the helpful comments which improved the quality of the manuscript. The authors thank Lucio Mayer for useful discussions and comments. D.I.V. and D.S. acknowledge the support from project *AYA2015-66211-C2-2 MINECO/FEDER, UE* of the Spanish Ministerio de Economía, Industria y Competitividad and the Aragón Government through the Research Groups E16.17R. D.I.V. particularly thanks the grant *Programa Operativo Fondo Social Europeo de Aragón 2014-2020 (Construyendo Europa desde Aragón)*. A.S. is supported by the ERC through the CoG grant 'B Massive', grant number 818691. Y.R.G. acknowledges the support of the European Research Council through grant number ERCStG/716151. S.B. and Y.R.G. acknowledge PGC2018-097585-B-C22, MINECO/FEDER, UE of the Spanish Ministerio de Economía, Industria y Competitividad. This work used the 2015 public version of the Munich model of galaxy formation and evolution: *L-Galaxies*. The source code and a full description of the model are available at <http://galformod.mpa-garching.mpg.de/public/LGalaxies/>. This work has made use of CEFCA's Scientific High Performance Computing system which has been funded by the Governments of Spain and Aragón through the Fondo de Inversiones de Teruel, and the Spanish Ministry of Economy and Competitiveness (MINECO-FEDER, grant AYA2012-30789).

REFERENCES

- Aird J., Coil A. L., Georgakakis A., Nandra K., Barro G., Pérez-González P. G., 2015, *MNRAS*, **451**, 1892
- Allevato V., et al., 2011, *ApJ*, **736**, 99
- Amaro-Seoane P., et al., 2017, arXiv e-prints,
- Angulo R. E., White S. D. M., 2010, *MNRAS*, **405**, 143
- Angulo R. E., White S. D. M., Springel V., Henriques B., 2014, *MNRAS*, **442**, 2131
- Antonini F., Barausse E., Silk J., 2015, *ApJ*, **812**, 72
- Athanassoula E., 2005, *MNRAS*, **358**, 1477
- Baker J. G., Boggs W. D., Centrella J., Kelly B. J., McWilliams S. T., Miller M. C., van Meter J. R., 2008, *ApJ*, **682**, L29
- Balbus S. A., Hawley J. F., 1998, *Reviews of Modern Physics*, **70**, 1
- Barausse E., 2012, *MNRAS*, **423**, 2533
- Barausse E., Rezzolla L., 2009, *ApJ*, **704**, L40
- Barausse E., Morozova V., Rezzolla L., 2012, *ApJ*, **758**, 63
- Bardeen J. M., 1970, *Nature*, **226**, 64
- Bardeen J. M., Petterson J. A., 1975a, *ApJ*, **195**, L65
- Bardeen J. M., Petterson J. A., 1975b, *ApJ*, **195**, L65
- Bardeen J. M., Press W. H., Teukolsky S. A., 1972, *ApJ*, **178**, 347
- Barnes J. E., Hernquist L. E., 1991, *ApJ*, **370**, L65
- Batta A., Ramirez-Ruiz E., Fryer C., 2017, *ApJ*, **846**, L15
- Begelman M. C., Blandford R. D., Rees M. J., 1980, *Nature*, **287**, 307
- Bekenstein J. D., 1973, *ApJ*, **183**, 657
- Bellovary J. M., Governato F., Quinn T. R., Wadsley J., Shen S., Volonteri M., 2010, *ApJ*, **721**, L148
- Berlind A. A., et al., 2003, *ApJ*, **593**, 1
- Bernardi M., Sheth R. K., Tundo E., Hyde J. B., 2007, *ApJ*, **660**, 267
- Berti E., Volonteri M., 2008, *ApJ*, **684**, 822
- Binney J., Tremaine S., 1987, Galactic dynamics
- Birzan L., Rafferty D. A., McNamara B. R., Wise M. W., Nulsen P. E. J., 2004, *ApJ*, **607**, 800
- Bischetti M., et al., 2017, *A&A*, **598**, A122
- Blandford R. D., Znajek R. L., 1977, *MNRAS*, **179**, 433
- Blecha L., Loeb A., 2008a, *MNRAS*, **390**, 1311
- Blecha L., Loeb A., 2008b, *MNRAS*, **390**, 1311
- Blecha L., Cox T. J., Loeb A., Hernquist L., 2011, *MNRAS*, **412**, 2154
- Bonetti M., Haardt F., Sesana A., Barausse E., 2018, *MNRAS*, **477**, 3910
- Bonetti M., Sesana A., Haardt F., Barausse E., Colpi M., 2019, *MNRAS*, **486**, 4044
- Bonoli S., Marulli F., Springel V., White S. D. M., Branchini E., Moscardini L., 2009, *MNRAS*, **396**, 423
- Bonoli S., Mayer L., Callegari S., 2014, *MNRAS*, **437**, 1576
- Bonoli S., Mayer L., Kazantzidis S., Madau P., Bellovary J., Governato F., 2016, *MNRAS*, **459**, 2603
- Bower R. G., Benson A. J., Malbon R., Helly J. C., Frenk C. S., Baugh C. M., Cole S., Lacey C. G., 2006, *MNRAS*, **370**, 645
- Boylan-Kolchin M., Ma C.-P., Quataert E., 2006, *MNRAS*, **369**, 1081
- Boylan-Kolchin M., Springel V., White S. D. M., Jenkins A., Lemson G., 2009, *MNRAS*, **398**, 1150
- Brennan L. W., Reynolds C. S., 2006, *ApJ*, **652**, 1028
- Buchner J., et al., 2015, *ApJ*, **802**, 89
- Bustamante S., Springel V., 2019, *MNRAS*, **490**, 4133
- Callegari S., Kazantzidis S., Mayer L., Colpi M., Bellovary J. M., Quinn T., Wadsley J., 2011a, *ApJ*, **729**, 85
- Callegari S., Kazantzidis S., Mayer L., Colpi M., Bellovary J. M., Quinn T., Wadsley J., 2011b, *ApJ*, **729**, 85
- Chandrasekhar S., 1943, *ApJ*, **97**, 255
- Chiaberge M., et al., 2017, *A&A*, **600**, A57
- Choksi N., Behroozi P., Volonteri M., Schneider R., Ma C.-P., Silk J., Moster B., 2017, *MNRAS*, **472**, 1526
- Civano F., et al., 2012, *ApJ*, **752**, 49
- Colless M., et al., 2001, *MNRAS*, **328**, 1039
- Colpi M., 2014, *Space Sci. Rev.*, **183**, 189
- Combes F., Sanders R. H., 1981, *A&A*, **96**, 164
- Contreras S., Zehavi I., Baugh C. M., Padilla N., Norberg P., 2017, *MNRAS*, **465**, 2833
- Cresci G., et al., 2015, *ApJ*, **799**, 82
- Croton D. J., 2006, *MNRAS*, **369**, 1808
- Cuadra J., Armitage P. J., Alexander R. D., Begelman M. C., 2009, *MNRAS*, **393**, 1423
- Debattista V. P., Mayer L., Carollo C. M., Moore B., Wadsley J., Quinn T., 2006, *ApJ*, **645**, 209
- Di Matteo T., Springel V., Hernquist L., 2005, *Nature*, **433**, 604
- Diamond-Stanic A. M., Rieke G. H., 2012, *ApJ*, **746**, 168
- Dotti M., Colpi M., Haardt F., Mayer L., 2007, *MNRAS*, **379**, 956
- Dotti M., Volonteri M., Perego A., Colpi M., Ruzszkowski M., Haardt F., 2010, *MNRAS*, **402**, 682
- Dotti M., Colpi M., Pallini S., Perego A., Volonteri M., 2013, *ApJ*, **762**, 68
- Du M., Debattista V. P., Shen J., Ho L. C., Erwin P., 2017, *ApJ*, **844**, L15

- Dubois Y., Devriendt J., Slyz A., Teyssier R., 2012, *MNRAS*, **420**, 2662
- Dubois Y., Volonteri M., Silk J., 2014, *MNRAS*, **440**, 1590
- Dubois Y., Volonteri M., Silk J., Devriendt J., Slyz A., Teyssier R., 2015, *Monthly Notices of the Royal Astronomical Society*, 452
- Dutton A. A., Macciò A. V., 2014, *MNRAS*, **441**, 3359
- Efstathiou G., Lake G., Negroponte J., 1982, *MNRAS*, **199**, 1069
- Eisenreich M., Naab T., Choi E., Ostriker J. P., Emsellem E., 2017, preprint, ([arXiv:1702.06965](https://arxiv.org/abs/1702.06965))
- Escala A., Larson R. B., Coppi P. S., Mardones D., 2004, *ApJ*, **607**, 765
- Escala A., Larson R. B., Coppi P. S., Mardones D., 2005, *ApJ*, **630**, 152
- Faber S. M., 1999, *Advances in Space Research*, **23**, 925
- Faltenbacher A., Mathews W. G., 2005, *MNRAS*, **362**, 498
- Fanali R., Dotti M., Fiacconi D., Haardt F., 2015, *MNRAS*, **454**, 3641
- Fanidakis N., Baugh C. M., Benson A. J., Bower R. G., Cole S., Done C., Frenk C. S., 2011, *MNRAS*, **410**, 53
- Fanidakis N., et al., 2012, *MNRAS*, **419**, 2797
- Fiacconi D., Mayer L., Roškar R., Colpi M., 2013, *ApJ*, **777**, L14
- Fiacconi D., Sijacki D., Pringle J. E., 2018, *MNRAS*, **477**, 3807
- Fuller J., Ma L., 2019, *ApJ*, **881**, L1
- Gardner J. P., et al., 2006, *Space Science Reviews*, **123**, 485
- Gerosa D., Sesana A., 2015, *MNRAS*, **446**, 38
- González J. A., Hannam M., Spherake U., Brüggmann B., Husa S., 2007, *Physical Review Letters*, **98**, 231101
- Greene J. E., Ho L. C., 2007, *ApJ*, **667**, 131
- Griffin A. J., Lacey C. G., Gonzalez-Perez V., Lagos C. d. P., Baugh C. M., Fanidakis N., 2019, *MNRAS*, **487**, 198
- Gualandris A., Merritt D., 2008, *ApJ*, **678**, 780
- Guedes J., Madau P., Mayer L., Callegari S., 2011, *ApJ*, **729**, 125
- Guo Q., et al., 2011, *MNRAS*, **413**, 101
- Haehnelt M. G., Rees M. J., 1993, *Monthly Notices of the Royal Astronomical Society*, 263, 168
- Häring N., Rix H.-W., 2004, *ApJ*, **604**, L89
- Hasinger G., Miyaji T., Schmidt M., 2005, *A&A*, **441**, 417
- Heavens A., Panter B., Jimenez R., Dunlop J., 2004, *Nature*, **428**, 625
- Heger A., Woosley S. E., 2002, *ApJ*, **567**, 532
- Henriques B. M. B., White S. D. M., Thomas P. A., Angulo R., Guo Q., Lemson G., Springel V., Overzier R., 2015, *MNRAS*, **451**, 2663
- Hernquist L., 1989, *Nature*, **340**, 687
- Hernquist L., 1990, *ApJ*, **356**, 359
- Hirschmann M., Somerville R. S., Naab T., Burkert A., 2012, *MNRAS*, **426**, 237
- Hirschmann M., Dolag K., Saro A., Bachmann L., Borgani S., Burkert A., 2014, *MNRAS*, **442**, 2304
- Hoffman L., Loeb A., 2007, *MNRAS*, **377**, 957
- Hopkins P. F., Quataert E., 2010, *MNRAS*, **407**, 1529
- Hopkins P. F., Hernquist L., Martini P., Cox T. J., Robertson B., Di Matteo T., Springel V., 2005, *ApJ*, **625**, L71
- Hopkins P. F., Hernquist L., Cox T. J., Robertson B., Di Matteo T., Springel V., 2006a, *ApJ*, **639**, 700
- Hopkins P. F., Narayan R., Hernquist L., 2006b, *ApJ*, **643**, 641
- Hopkins P. F., Richards G. T., Hernquist L., 2007, *ApJ*, **654**, 731
- Hopkins P. F., Cox T. J., Younger J. D., Hernquist L., 2009, *ApJ*, **691**, 1168
- Hut P., Rees M. J., 1992, *MNRAS*, **259**, 27P
- Izquierdo-Villalba D., Bonoli S., Spinoso D., Rosas-Guevara Y., Henriques B. M. B., Hernández-Monteagudo C., 2019, *MNRAS*, **488**, 609
- Kalfountzou E., Santos Lleo M., Trichas M., 2017, *ApJ*, **851**, L15
- Kauffmann G., Haehnelt M., 2000, *MNRAS*, **311**, 576
- Kelley L. Z., Blecha L., Hernquist L., 2017a, *MNRAS*, **464**, 3131
- Kelley L. Z., Blecha L., Hernquist L., Sesana A., Taylor S. R., 2017b, *MNRAS*, **471**, 4508
- King A. R., Pringle J. E., 2006, *Monthly Notices of the Royal Astronomical Society: Letters*, 373, L90
- King A. R., Pringle J. E., 2007, *MNRAS*, **377**, L25
- King A. R., Lubow S. H., Ogilvie G. I., Pringle J. E., 2005, *MNRAS*, **363**, 49
- King A. R., Pringle J. E., Hofmann J. A., 2008, *MNRAS*, **385**, 1621
- Komossa S., 2012, *Advances in Astronomy*, 2012, 364973
- Kormendy J., Ho L. C., 2013, *ARA&A*, **51**, 511
- Koushiappas S. M., Bullock J. S., Dekel A., 2004, *MNRAS*, **354**, 292
- Lagos C. D. P., Cora S. A., Padilla N. D., 2008, *MNRAS*, **388**, 587
- Lena D., Robinson A., Marconi A., Axon D. J., Capetti A., Merritt D., Batcheldor D., 2014, *ApJ*, **795**, 146
- Li Y., et al., 2007, *ApJ*, **665**, 187
- Loeb A., 2007, *Phys. Rev. Lett.*, **99**, 041103
- Lousto C. O., Zlochower Y., 2008, *Phys. Rev. D*, **77**, 044028
- Lousto C. O., Zlochower Y., Dotti M., Volonteri M., 2012, *Phys. Rev. D*, **85**, 084015
- Madau P., Quataert E., 2004, *ApJ*, **606**, L17
- Madau P., Rees M. J., 2001, *ApJ*, **551**, L27
- Marconi A., Risaliti G., Gilli R., Hunt L. K., Maiolino R., Salvati M., 2004, *MNRAS*, **351**, 169
- Marian V., et al., 2019, *ApJ*, **882**, 141
- Marshall M. A., Mutch S. J., Qin Y., Poole G. B., Wytthe J. S. B., 2020, *MNRAS*, **494**, 2747
- Martel H., Barai P., Brito W., 2012, *ApJ*, **757**, 48
- Martin G., et al., 2018, *MNRAS*, **476**, 2801
- Marulli F., Bonoli S., Branchini E., Moscardini L., Springel V., 2008, *MNRAS*, **385**, 1846
- Mayer L., 2013, *Classical and Quantum Gravity*, **30**, 244008
- Mayer L., Bonoli S., 2019, *Reports on Progress in Physics*, **82**, 016901
- Mayer L., Kazantzidis S., Escala A., Callegari S., 2010, *Nature*, **466**, 1082
- Menci N., Gatti M., Fiore F., Lamastra A., 2014, *A&A*, **569**, A37
- Méndez-Abreu J., Sánchez-Janssen R., Aguerri J. A. L., 2010, *ApJ*, **711**, L61
- Merloni A., Heinz S., 2008, *MNRAS*, **388**, 1011
- Merloni A., Rudnick G., Di Matteo T., 2004, *MNRAS*, **354**, L37
- Mihos J. C., Hernquist L., 1996, *ApJ*, **464**, 641
- Miki Y., Mori M., Kawaguchi T., Saito Y., 2014, *ApJ*, **783**, 87
- Mo H. J., Mao S., White S. D. M., 1998, *MNRAS*, **295**, 319
- Mo H., van den Bosch F. C., White S., 2010, *Galaxy Formation and Evolution*
- Moetazedian R., Polyachenko E. V., Berczik P., Just A., 2017, *A&A*, **604**, A75
- Moore B., Ghigna S., Governato F., Lake G., Quinn T., Stadel J., Tozzi P., 1999, *ApJ*, **524**, L19
- Mullaney J. R., et al., 2012a, *MNRAS*, **419**, 95
- Mullaney J. R., et al., 2012b, *ApJ*, **753**, L30
- Nandra K., et al., 2013, arXiv e-prints, [p. arXiv:1306.2307](https://arxiv.org/abs/1306.2307)
- Narayan R., Yi I., 1994, *ApJ*, **428**, L13
- Navarro J. F., Frenk C. S., White S. D. M., 1996, *ApJ*, **462**, 563
- Novikov I. D., Thorne K. S., 1973, in *Black Holes (Les Astres Occlus)*. pp 343–450
- O’Dowd M., Urry C. M., Scarpa R., 2002, *ApJ*, **580**, 96
- Orban de Xivry G., Davies R., Schartmann M., Komossa S., Marconi A., Hicks E., Engel H., Tacconi L., 2011, *MNRAS*, **417**, 2721
- Pacucci F., Ferrara A., 2015, *MNRAS*, **448**, 104
- Page D. N., Thorne K. S., 1974, *ApJ*, **191**, 499
- Perego A., Dotti M., Colpi M., Volonteri M., 2009, *MNRAS*, **399**, 2249
- Pfenniger D., Norman C., 1990, *ApJ*, **363**, 391

Pfister H., Volonteri M., Dubois Y., Dotti M., Colpi M., 2019, *MNRAS*, **486**, 101

Planck Collaboration et al., 2014, *A&A*, **571**, A16

Postman M., et al., 2012, *ApJ*, **756**, 159

Press W. H., Schechter P., 1974, *ApJ*, **187**, 425

Quinlan G. D., Hernquist L., 1997, *New Astron.*, **2**, 533

Redmount I. H., Rees M. J., 1989, *Comments on Astrophysics*, **14**, 165

Rees M. J., Begelman M. C., Blandford R. D., Phinney E. S., 1982, *Nature*, **295**, 17

Reynolds C. S., 2013, *Classical and Quantum Gravity*, **30**, 244004

Rosas-Guevara Y., Bower R. G., Schaye J., McAlpine S., Dalla Vecchia C., Frenk C. S., Schaller M., Theuns T., 2016, *MNRAS*, **462**, 190

Rosas-Guevara Y., et al., 2020, *MNRAS*, **491**, 2547

Roulet J., Zaldarriaga M., 2019, *MNRAS*, **484**, 4216

Savorgnan G. A. D., Graham A. W., Marconi A. r., Sani E., 2016, *ApJ*, **817**, 21

Schmidt M., 1963, *Nature*, **197**, 1040

Schulze A., Wisotzki L., 2010, *A&A*, **516**, A87

Sellwood J. A., 2016, *ApJ*, **819**, 92

Sesana A., 2013, *Monthly Notices of the Royal Astronomical Society: Letters*, **433**, L1

Sesana A., Barausse E., Dotti M., Rossi E. M., 2014, *ApJ*, **794**, 104

Sesana A., Shankar F., Bernardi M., Sheth R. K., 2016, *MNRAS*, **463**, L6

Shakura N. I., Sunyaev R. A., 1973, *A&A*, **24**, 337

Shankar F., Salucci P., Granato G. L., De Zotti G., Danese L., 2004, *MNRAS*, **354**, 1020

Shankar F., Weinberg D. H., Miralda-Escudé J., 2009, *ApJ*, **690**, 20

Shankar F., et al., 2016, *MNRAS*, **460**, 3119

Shankar F., et al., 2019, *MNRAS*, **485**, 1278

Shlosman I., Begelman M. C., 1989, *ApJ*, **341**, 685

Shlosman I., Frank J., Begelman M. C., 1989, *Nature*, **338**, 45

Sijacki D., Springel V., Haehnelt M. G., 2009, *MNRAS*, **400**, 100

Silk J., Rees M. J., 1998, *A&A*, **331**, L1

Small T. A., Blandford R. D., 1992, *Monthly Notices of the Royal Astronomical Society*, **259**, 725

Smethurst R. J., Simmons B. D., Lintott C. J., Shanahan J., 2019, *MNRAS*, **489**, 4016

Soltan A., 1982, *MNRAS*, **200**, 115

Spinoso D., Bonoli S., Dotti M., Mayer L., Madau P., Bellovary J., 2017, *MNRAS*, **465**, 3729

Springel V., 2005, *MNRAS*, **364**, 1105

Springel V., White S. D. M., Tormen G., Kauffmann G., 2001, *MNRAS*, **328**, 726

Steinborn L. K., Hirschmann M., Dolag K., Shankar F., Juneau S., Krumpke M., Remus R.-S., Teklu A. F., 2018, *MNRAS*, **481**, 341

Tamburello V., Capelo P. R., Mayer L., Bellovary J. M., Wadsley J. W., 2017, *MNRAS*, **464**, 2952

Tanaka T., Haiman Z., 2009, *ApJ*, **696**, 1798

Thomas N., Davé R., Anglés-Alcázar D., Jarvis M., 2019, *MNRAS*, **487**, 5764

Thompson T. A., Quataert E., Murray N., 2005, *ApJ*, **630**, 167

Thorne K. S., 1974, *ApJ*, **191**, 507

Tichy W., Marronetti P., 2008, *Phys. Rev. D*, **78**, 081501

Tombesi F., Tazaki F., Mushotzky R. F., Ueda Y., Cappi M., Gofford J., Reeves J. N., Guainazzi M., 2014, *MNRAS*, **443**, 2154

Tombesi F., Meléndez M., Veilleux S., Reeves J. N., González-Alfonso E., Reynolds C. S., 2015, *Nature*, **519**, 436

Trakhtenbrot B., 2014, *ApJ*, **789**, L9

Tremmel M., Governato F., Volonteri M., Pontzen A., Quinn T. R., 2018, *ApJ*, **857**, L22

Trujillo I., Ferreras I., de La Rosa I. G., 2011, *MNRAS*, **415**, 3903

Ueda Y., Akiyama M., Hasinger G., Miyaji T., Watson M. G., 2014, *ApJ*, **786**, 104

Volonteri M., 2010, *A&ARv*, **18**, 279

Volonteri M., Madau P., 2008, *The Astrophysical Journal*, **687**, L57

Volonteri M., Perna R., 2005, *MNRAS*, **358**, 913

Volonteri M., Stark D. P., 2011, *MNRAS*, **417**, 2085

Volonteri M., Haardt F., Madau P., 2003, *ApJ*, **582**, 559

Volonteri M., Sikora M., Lasota J.-P., 2007, *ApJ*, **667**, 704

Volonteri M., Sikora M., Lasota J.-P., Merloni A., 2013, *ApJ*, **775**, 94

Volonteri M., Silk J., Dubus G., 2015, *ApJ*, **804**, 148

White S. D. M., Rees M. J., 1978, *MNRAS*, **183**, 341

Zackay B., Venumadhav T., Dai L., Roulet J., Zaldarriaga M., 2019, *Phys. Rev. D*, **100**, 023007

Zana T., Dotti M., Capelo P. R., Bonoli S., Haardt F., Mayer L., Spinoso D., 2018a, *MNRAS*, **473**, 2608

Zana T., Dotti M., Capelo P. R., Mayer L., Haardt F., Shen S., Bonoli S., 2018b, *MNRAS*, **479**, 5214

del Valle L., Escala A., Maureira-Fredes C., Molina J., Cuadra J., Amaro-Seoane P., 2015, *ApJ*, **811**, 59

eLISA Consortium et al., 2013, arXiv e-prints, p. arXiv:1305.5720

van Meter J. R., Miller M. C., Baker J. G., Boggs W. D., Kelly B. J., 2010, *ApJ*, **719**, 1427

APPENDIX A: EJECTIONS VIA GRAVITATIONAL RECOIL AND THREE BODY SCATTERING

As we have discussed in Section 3.4 nuclear BHs can be expelled from the galaxy nuclear region through both gravitational recoils and recoils after 3-body scattering. While the former is led by the final BH-BH coalescence, the latter is the consequence of a complex interaction between a binary BH system and an intruder BH which causes the ejection of the less massive BH. In this appendix, we show that the ejections after a gravitational recoil are more common than the ejections via 3-body scattering. Thus, the population of *ejected* wBHs is fully dominated by gravitational recoiled BHs. To prove so, in Figure A1 we present the evolution of the number density (n) of ejections through gravitational ejection and 3-body scattering. As shown, at $M_{\text{halo}} > 10^{11} M_{\odot}$ ejections after gravitational recoils dominate the ejected population, being 1–2 dex more frequent at any redshift. As we can see, the ejection after 3-body scattering is dominated by low mass BHs ($M_{\text{BH}} < 10^6 M_{\odot}$) at any redshift and subhalo mass. On the other hand, the ejection of BHs of $M_{\text{BH}} > 10^8 M_{\odot}$ after a 3-body scattering is relatively rare, with less than 300 events at $z < 2$. These events happen mainly in $M_{\text{halo}} > 10^{13} M_{\odot}$, which are the ones hosting the galaxies with the most massive BHs in the SAM.

APPENDIX B: X-RAY LUMINOSITY FUNCTIONS

The redshift evolution of X-ray luminosity functions is presented in Fig.B1 and Fig.B2. Soft (0.5–2 keV) and hard (2–10 keV) X-ray luminosity have been computed by using the bolometric corrections derived in Marconi et al. (2004):

$$\log_{10} (L_{\text{Hx}}/L_{\text{bol}}) = -1.54 - 0.24\mathcal{L} - 0.012\mathcal{L}^2 + 0.0015\mathcal{L}^3 \quad (\text{B1})$$

$$\log_{10} (L_{\text{Sx}}/L_{\text{bol}}) = -1.64 - 0.22\mathcal{L} - 0.012\mathcal{L}^2 + 0.0015\mathcal{L}^3 \quad (\text{B2})$$

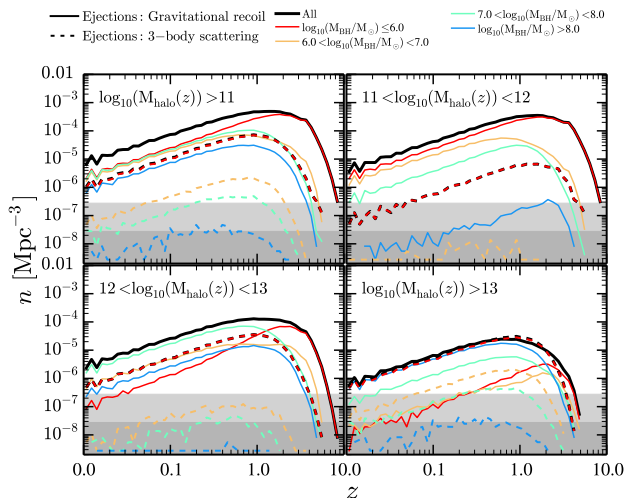


Figure A1. Number density (n) of nuclear black holes that are ejected from the nuclear part of the galaxy. Each panel represents a bin of subhalo mass (M_{halo}). While solid lines display the ejections caused by gravitational recoils, dashed ones display the same but for BHs that were ejected via 3-body scattering. Colors represent different bins of BH mass. With shaded areas it is highlighted the value of n in which we have less than 100 (faint grey) and 10 (dark grey) events.

where $\mathcal{L} = \log_{10}(L_{\text{bol}}/L_{\odot}) - 12$, L_{HX} is the hard X-ray luminosity and L_{SX} soft X-ray luminosity. Predictions are compared to the observational works of Ueda et al. (2014) Aird et al. (2015) and Buchner et al. (2015). Given the uncertainty in modelling the fraction of obscured AGNs, we prefer to compare the simulations to Aird et al. (2015) observed soft X-ray luminosity functions for which the obscured fraction has already been taken into account. The fraction of obscured objects in the hard X-ray band is thought to be relatively small, so for this work we consider that there is no obscuration at hard X-ray wavelengths. As we can see, good agreement between observations and model is reached. In the same figures we have divided the population between elliptical, classical bulges and pseudobulges. As we found with the bolometric luminosity, at $z \gtrsim 2$ the luminosity functions are dominated by BHs accreting in pseudobulges structures. On contrary, at $z \lesssim 1$ classical bulges and elliptical galaxies are the structures that preferentially host AGNs and quasars.

This paper has been typeset from a $\text{T}_{\text{E}}\text{X}/\text{L}^{\text{A}}\text{T}_{\text{E}}\text{X}$ file prepared by the author.

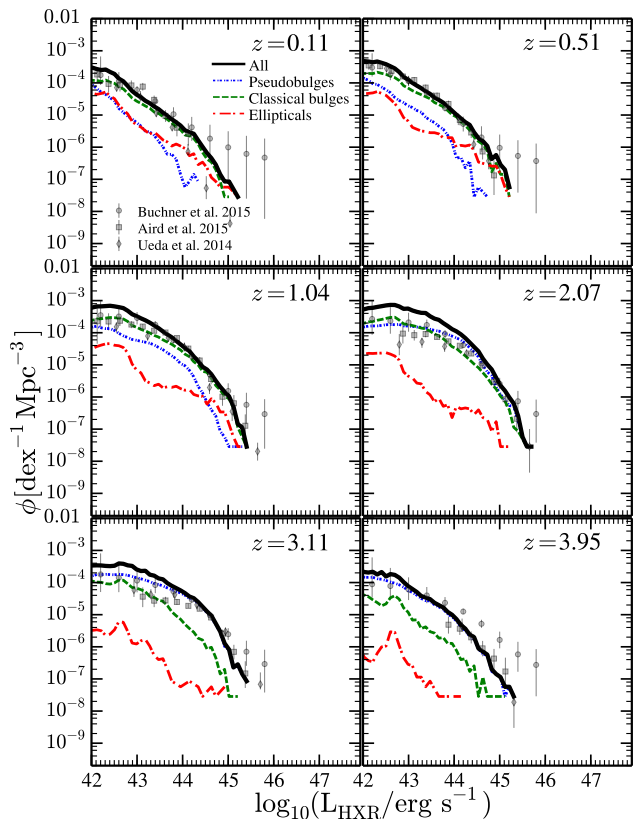


Figure B1. X-ray luminosity functions at $z \approx 0.1, 0.5, 1.0, 2.0, 3.0, 4.0$. In solid black line we present the predicted hard X-ray (2–10 keV) luminosity functions. Red dashed-dotted line, green dashed line, and blue dotted line represents the luminosity functions for galaxies hosting, respectively, elliptical, classical bulge, and pseudobulge structure. Each luminosity function is compared with the compilation of Buchner et al. (2015); Aird et al. (2015); Ueda et al. (2014) (circle, square and, diamond points, respectively).

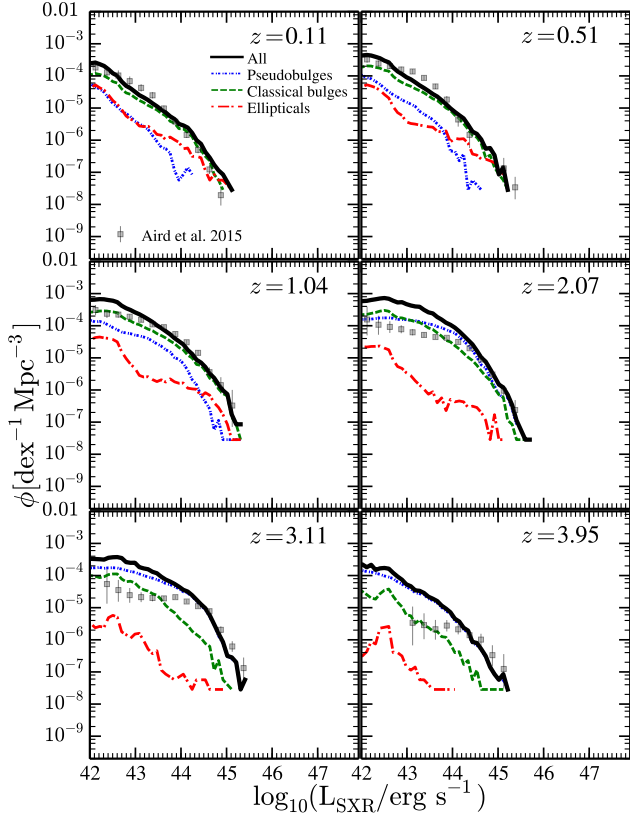


Figure B2. X-ray luminosity functions at $z \approx 0.1, 0.5, 1.0, 2.0, 3.0, 4.0$. In solid black line we present the predicted *soft* X-ray (0.5-2 keV) luminosity functions. Each luminosity functions is compared with the compilation of [Buchner et al. \(2015\)](#); [Aird et al. \(2015\)](#); [Ueda et al. \(2014\)](#) (circle, square and, diamond points, respectively).